European Journal of Control 69 (2023) 100738

Contents lists available at ScienceDirect

European Journal of Control

journal homepage: www.elsevier.com/locate/ejcon

Comparative study of post-impact motion control of a flexible arm space robot

Sharmila Kayastha[a,*], Jayantha Katupitiya[b], Garth Pearce[b], Asha Rao[a]

[a] Mathematical Sciences Discipline, School of Science, RMIT University, Australia
[b] School of Mechanical and Manufacturing Engineering, University of New South Wales, Australia

ARTICLE INFO

Article history:
Received 14 September 2021
Revised 13 August 2022
Accepted 31 August 2022
Available online 7 September 2022

Recommended by Prof. T Parisini

Keywords:
Post-impact dynamics of space robot
Motion control
Nonlinear model predictive control
Sliding mode control
Linear quadratic regulator

ABSTRACT

Designing a controller to manipulate a flexible space robot is hampered by the inherent complex nonlinear dynamics. Furthermore, the collision of a space robot with an external object in the space environment often leads to degradation of the space robot system. Therefore, an effective control algorithm is necessary for a successful space robot mission to regulate the motion of the entire system after an impact. This paper presents a comparative study on the performance of two different composite controllers to control post-impact motion of the space robot with two-link flexible arms. A performance comparison study helps to choose a better controller to carry out specific tasks. The dynamics of a space robot with flexible manipulators are highly nonlinear and coupled, hence split into rigid and flexible motion to make the control design easier. In this paper, two different composite controllers, namely Nonlinear Model Predictive Control with a Linear Quadratic Regulator (NMPC-LQR) and Sliding Mode Control with Linear Quadratic Regulator (SMC-LQR) are developed. NMPC and SMC are used to control rigid motion of the system, while LQR is used to suppress the flexible motion. The objective of the proposed controllers is to regulate the motion of the entire space robot system, including the flexible manipulator, after impact with an external object. The effectiveness of the proposed composite controllers is demonstrated using numerical simulations. Simulation results confirm that, in the absence of uncertainties, the performance of the control system using the proposed NMPC-LQR is more accurate compared to using SMC-LQR. Furthermore, given uncertainties of mass and inertia of the system, we find NMPC-LQR provides a higher level of accuracy when compared to SMC-LQR.

1. Introduction

Space robots are and will continue to be essential for future space missions [28] to conduct on-orbit servicing tasks telerobotically or autonomously instead of the current repetitious, unsafe and high-cost astronaut extravehicular activities. To carry out such activities successfully in the space environment, space systems require robots with higher speed, lower manipulation cost, better maneuverability and lighter weight. Consequently, space robots with flexible manipulator are preferable for carrying out space robot missions [23,52]. Several control schemes proposed in the literature show successful results on system modeling and control of space robots with a rigid arm, as well as of single link flexible space robots [8,15,24,43,51–53]. However, flexible link dynamics is often neglected in existing research due to challenges in developing the dynamic equations of space robotic manipulators and designing the effective control law. The control law used for rigid manipulators does not effectively track the desired trajectory of a system with flexible robot arms, and research is growing on space robots with flexible manipulator, and on the control of multi-arm flexible space robots to improve the performance of these robots [23,51,52]. In [23], a review of kinematic analysis and different control methods of space flexible manipulators is given, along with the many, different problems associated with them. In [51,52], dynamic modelling and control of a space robot with multi-arm flexible links is proposed. The literature [23,51,52] shows the effectiveness of the proposed control schemes to track both rigid and flexible motion of the space robot system. However, none of the above articles, and references therein, deal with post-impact dynamics of a spacecraft with multi-arm flexible robot.

While performing space robot applications, the space robot might collide with an external object, such as space debris, in the space environment, resulting in undesirable performance and, possibly, catastrophic damage. This leads to high mission costs, increased turn-around time or could even cause the mission to be aborted [39]. Space debris includes natural debris, such as

* Corresponding author.
E-mail address: sharmila.kayastha@rmit.edu.au (S. Kayastha).

https://doi.org/10.1016/j.ejcon.2022.100738

meteoroids, as well as artificial debris, such as malfunctioning spacecrafts, launch vehicles left behind, and fragmentation debris. As space junk increases, collisions will become more common, and so will the need to develop effective control schemes to control the motion of the entire system before and after impact. Such collisions could lead to high impact events, as both space debris and spacecraft travel with very high speeds.

The impact dynamics and post-impact motion control of a flexible dual-arm space robot system was investigated in [29,30] for capturing a stationary object as well as a spinning object. The simulation results verified that the proposed PD controller stabilized the space robot system and the flexible motion of the space robots. However, in [29,30], only the forearms of the space robot were taken to be flexible. A continuous contact force was used to define the collision process in [2] and the detrimental effects on space flexible manipulators reduced by employing a contact force minimization strategy to carry out desired tasks. Hence, most research has, thus far, investigated the post-impact dynamics and control of a space robot either with rigid arms or with only the forearm being flexible.

A detailed survey on robotic manipulation and capture in space environment was undertaken in [39]. The authors, Papadapolous et al., provide lists of articles dealing with the dynamics of both rigid and flexible manipulators in orbit, contact dynamics between manipulators, grippers and their targets, as well as motion planning and control methods. The reader is referred to this survey paper and the lists of references therein [39]. The dynamic modeling and vibration analysis of a space manipulator with flexible link and flexible joint is investigated in [37]. In [26], an existing space robot system with rigid arms or with only the forearm being flexible, was enhanced by using a two-link flexible manipulator. A composite controller, SMC-LQR, was developed in [26] to control the unstable motion of the entire space robot with flexible manipulator (SRFM) after impact with an external object. However, the controller in [26] was found to be not suitable for tasks requiring higher accuracy such as fuelling and painting, thus motivating the design of a more effective control law that provides higher accuracy.

The main purpose of this work is a performance comparison of the space robot with two-link flexible manipulator using two different composite controllers both in the presence and the absence of uncertainties. As mentioned earlier, the comparative study helps the designer to select the best controller based on the requirements. In this research, the space robot with a two-link flexible manipulator developed in [26] is used. As the system dynamics of the SRFM are highly nonlinear, it is separated into rigid and flexible motions to make designing the control law easier. Here, NMPC is used to control the rigid motion of the system while the flexible motion of the system is controlled using LQR. Previous research has used NMPC for space robots with only rigid manipulators. NMPC guarantees high fidelity due to its predictive nature and receding horizon optimization technique [16]. Therefore, in this study, a composite controller, NMPC-LQR, is developed to control the post-impact motion of the space robot with two-link flexible manipulator and the performance is compared with the SMC-LQR controller proposed in [26]. Numerical simulations show that the proposed NMPC-LQR performs better than the SMC-LQR presented in [26]. This performance comparison study provides an option to select an appropriate controller based on requirement such as higher accuracy.

The rest of this paper is organized as follows: Section 2 provides background on the different control methods used in recent literature to control the motion of an SRFM. The post-impact dynamic equations of the SRFM and the dynamic equations of the impact object are presented in Section 3. Section 4 shows the detailed derivations to separate the dynamic equation of the system into rigid motion and flexible motion. Section 5 includes the derivation of two different composite control techniques for post-impact motion control of SRFM. In Section 6, the effectiveness of the proposed composite controllers, are verified via numerical simulations and the performance of the system using the two control methods compared. Section 7 concludes the paper.

2. Background

The control systems of space robots are different from ground robots as space robots need to operate in a different environment compared to ground robots. In the space environment there is no air, but there is radiation, extreme temperatures, and changing illumination conditions. Also, the absence of gravitational forces makes moving in space tricky and gives rise to unique challenges not experienced by ground robots. Space robots can be either free-flying or free-floating in a space environment while being attached to a spacecraft base. In this scenario, the movements of the manipulator disturb the spacecraft base because of the coupling mechanism [14]. These disturbances cause undesirable movements in a spacecraft base, which may disrupt communication between space and ground systems, as well as solar energy collection. In addition, the coupling mechanism and the nonlinear behavior of the system creates difficulty in developing system dynamics and control law [12,48]. Hence, the space robot system may fail to track the end-effector trajectory with high enough accuracy. This means the spacecraft will fail to perform the desired task as it is coupled with the space robotic arms. The end-effector of a space robot may be impacted by external objects during certain operations, such as removal of space debris, collection of disabled satellites, docking with other spacecraft, etc. [5,47]. The impact of an external object disturbs the motion of both the spacecraft base and the robotic manipulator. It might damage the space robot system leading to undesirable motion in the system [7,30,38]. Therefore, it is essential to develop effective controllers to control both the pre-impact and post-impact motion of space robot system.

Using effective control laws helps to minimize the effect of collision with an external object in the space environment as the controller helps to follow the desired trajectory of the system by minimizing the error between actual and desired values. Normally, there should be no relative velocities between the end-effector of the space robot and the external object, however, this is not practically achievable [30]. During impact, the end-effector interacts with the external object and impact forces are produced. Post-impact dynamics are developed for the combined space robot system and the object by determining the change in generalized velocities [41]. However, a normal control system will not perform well after an impact if impact dynamics are not considered. Hence, for a successful space robot mission, both the translational and rotational motion of the base, along with the motion of the robotic manipulator, must be controlled before and after impact. An effective control method has been proposed in [41] to perform post capture operations such as repairing satellites without being disturbed by base reactions, and moving a captured object to the desired location. Also, in the space environment, uncertainties and disturbances, such as space debris, radiation, collision with other spacecrafts, are always present and hence could affect the performance of a space robot system. Therefore, space robot systems with flexible joints can be used to cope with these uncertainties [33]. There is some research [4,50] that includes flexible, instead of rigid, joints to improve the tracking performance in the presence of time varying uncertainty parameters. The readers are referred to the references within these articles [4,50] to learn more about flexible joints. However, in this research the flexibility of the joints is ignored.

Several studies [34–36,51,54–56] suggest the use of perturbation to control the motion of an SRFM. In this technique, the highly nonlinear dynamic equations of the SRFM are separated into rigid and flexible subsystems. To control rigid motion, several control techniques including online feedback tracking control based on Lyapunov-like methodology [3], composite adaptive controller [55], adaptive SMC [51], and an augmented robust control [54] have been developed. The LQR method is used to suppress the vibration of the flexible manipulators, and satisfactory simulation results are achieved using the proposed composite controllers. However, none of this research deals with post-impact motion control of a space robot with both links flexible.

As mentioned earlier, most existing research focuses on post-impact motion control of a space robot either with all rigid arms or only the forearm being flexible. Research dealing with post-impact dynamics and control of a rigid arm space robot can be found in [6,7,21,22,38,41]. A reaction null space concept is proposed in [38] to control post-impact dynamics of a free-floating space robot subject to a force impulse. In [7], a robust adaptive compound control algorithm is developed to suppress the unstable motion produced by impact, on a space robot with rigid manipulators. Two different controllers namely distributed momentum control and reaction null space control methods are proposed in [6] for 3 degrees of freedom (DOF) planar manipulator of a free-floating space robot system.

In [29,30], only the forearm was flexible, even though a flexible dual-arm space robot was studied. Furthermore, some papers studying post-impact dynamics [7,38] only consider attitude control, ignoring position control of the spacecraft base. This results in failure of the end-effector to reach the specified trajectory as both the attitude angle and the position of the spacecraft base disturb the robot manipulator. Therefore, it is necessary to develop an accurate model of the pre-impact and post-impact dynamics of the SRFM system and to design effective control techniques regulating both the rotational and translational motion of both spacecraft and flexible manipulator accurately and simultaneously, which is the aim of this research.

This paper presents a derivation of the post-impact dynamic model of the space robot with two-link flexible manipulator based on the momentum conservation principle. The highly nonlinear and coupled dynamic equations of a flexible space robot system makes control design difficult. In this study, to make designing the controller easier, a planar SRFM is considered and highly nonlinear coupled dynamics are separated into rigid and flexible subsystems. The derivation of the composite controller NMPC-LQR is shown to be better at controlling the motion of the space robot system after impact with an external object when in orbit. In predictive control law, the predicted tracking error is minimized over a fixed time horizon. According to [16], NMPC ensures high accuracy in trajectory tracking due to the receding optimization and predictive nature of the algorithm. In [20], one step ahead robust MPC is proposed for LPV model with bounded disturbance, with the effectiveness of the proposed online approach compared to offline approach illustrated. In [1,16], one step ahead NMPC is used successfully for trajectory tracking of ground robots.

Over the past two decades, NMPC has been successfully implemented in various ground robot applications [1,11,12,16–18,40,57]. These applications have been extended to space robots with rigid manipulators [25,42,45]. In these latter articles, NMPC is shown to produce satisfactory performance in controlling the motion of a space robot system with rigid manipulator. Extending these in a natural way, in this paper, the NMPC control technique in combination with LQR, implemented to control post-impact motion of a space robot system with both links flexible, is shown to have higher accuracy in carrying out space robot missions. We conduct numerical simulations using NMPC-LQR comparing the post-impact motion control of a space robot system with two-link flexible manipulator with the SMC-LQR proposed in [26]. In addition, the parametric uncertainty of mass and moment of inertia of SRFM is considered and the results of numerical simulations presented.

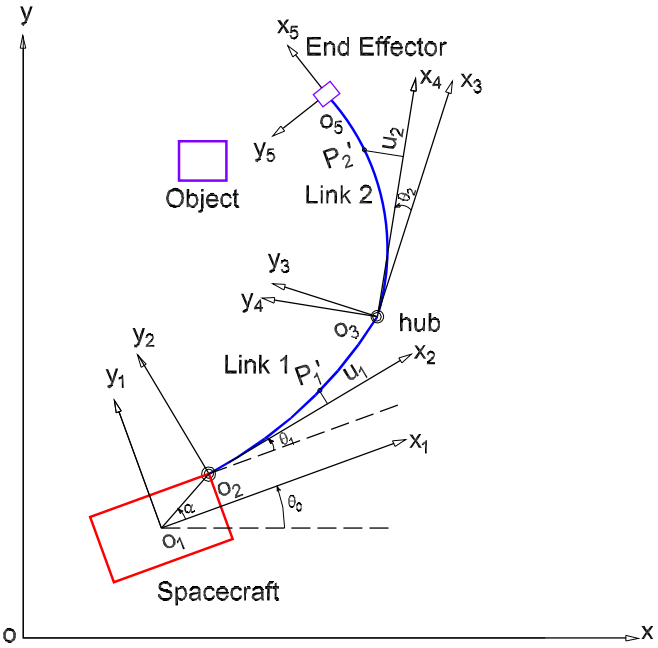

Fig. 1. Schematic of planar SRFM and object in space environment [26]. The arm is manueuvred by two joint motors by applying torques at each joint respectively.

3. System modelling

This section describes the equations of motion of the SRFM. In this study, the two-link flexible manipulator mounted on a rigid spacecraft base, as shown in Fig. 1, is used. The final dynamic equations of a space robot with a flexible manipulator are derived using the Assumed Mode Method (AMM) and the Lagrangian equation as given in [3,35,51]. The system dynamics of the external object is used to derive the post-impact dynamics of the whole system. However, the properties of the external object may or may not be known prior to impact. If the space robots are used to connect with another spacecraft these properties are known but, are unknown if the space robots collide with other free flying space debris and spacecrafts. Before deriving the system dynamics, the following assumptions are made:

1. The flexible links are assumed to be Euler-Bernoulli Beams. Therefore, the rotational inertia and shear deformation are neglected.
2. The flexibility of the joints are ignored.

3.1. Kinematics

The motions of the system are defined by various coordinate frames (refer to Fig. 1) and are given as (see [3] for more details): inertial coordinate frame $\sum_0 xoy$, spacecraft base frame $\sum_1 x_1o_1y_1$, rigid body moving frames $\sum_2 x_2o_2y_2$, and $\sum_4 x_4o_3y_4$ for links 1 and 2, respectively, and flexible body moving frames $\sum_3 x_3o_3y_3$ and $\sum_5 x_5o_5y_5$ for links 1 and 2, respectively. The position vector and the orientation of the spacecraft base are defined by $[x_b; y_b; \theta_0]$. Similarly, the joint angles $[\theta_1; \theta_2]$ define the rigid motions of the manipulator, and the flexible deflection of the link at two arbitrary points P_1' and P_2' is given by $[u_1; u_2]$, respectively. The masses m_b, m_{L1}, m_{L2}, m_H, and m_E represent those of spacecraft base, link 1,

link 2, hub, and payload(end-effector), respectively. The distance between o_1o_2 is L_b, and L_i is the length of link i where $i = 1, 2$. The inertia of the spacecraft base, hub, and payload are defined by I_b, I_H, I_E, respectively and α denotes $\angle x_1 o_1 o_2$.

The relationship among the coordinate systems is given by respective transformation matrices. The rigid rotation matrix $\boldsymbol{R}_{ri}(\theta_i)$ for rigid motion is defined as in [3,51]

$$\boldsymbol{R}_{ri}(\theta_i) = \begin{bmatrix} \cos\theta_i & -\sin\theta_i \\ \sin\theta_i & \cos\theta_i \end{bmatrix}, i = 0, 1, 2. \tag{1}$$

Similarly, for the flexible motion, the flexible deflection rotation matrix at the end of the flexible link is,

$$\boldsymbol{R}_{fj}(u_{je}) = \begin{bmatrix} 1 & -u'_{je} \\ u'_{je} & 1 \end{bmatrix}, j = 1, 2, \tag{2}$$

where $u'_j = \dfrac{\partial u_j}{\partial x_{Li}}$. The displacement vector of the system with respect to the inertial coordinate frame can be written as,

$$\boldsymbol{r}_b = \begin{bmatrix} x_b & y_b \end{bmatrix}^T, \tag{3}$$

$$\boldsymbol{r}_{P1} = \begin{bmatrix} x_b + L_b c_{0\alpha} + x_{L1} c_{01\alpha} - u_1 s_{01\alpha} \\ y_b + L_b s_{0\alpha} + x_{L1} s_{01\alpha} + u_1 c_{01\alpha} \end{bmatrix}, \tag{4}$$

$$\boldsymbol{r}_H = \begin{bmatrix} x_b + L_b c_{0\alpha} + L_1 c_{01\alpha} - u_{1e} s_{01\alpha} \\ y_b + L_b s_{0\alpha} + L_1 s_{01\alpha} + u_{1e} c_{01\alpha} \end{bmatrix}, \tag{5}$$

$$\begin{aligned} \boldsymbol{r}_{P2} = & \begin{bmatrix} x_b + L_b c_{0\alpha} + L_1 c_{01\alpha} - u_{1e} s_{01\alpha} \\ y_b + L_b s_{0\alpha} + L_1 s_{01\alpha} + u_{1e} c_{01\alpha} \end{bmatrix} \\ & + \begin{bmatrix} x_{L2}(c_{012\alpha} - u'_{1e} s_{012\alpha}) - u_2(u'_{1e} c_{012\alpha} + s_{012\alpha}) \\ x_{L2}(s_{012\alpha} + u'_{1e} c_{012\alpha}) + u_2(-u'_{1e} s_{012\alpha} + c_{012\alpha}) \end{bmatrix}, \end{aligned} \tag{6}$$

$$\begin{aligned} \boldsymbol{r}_E = & \begin{bmatrix} x_b + L_b c_{0\alpha} + L_1 c_{01\alpha} - u_{1e} s_{01\alpha} \\ y_b + L_b s_{0\alpha} + L_1 s_{01\alpha} + u_{1e} c_{01\alpha} \end{bmatrix} \\ & + \begin{bmatrix} L_2(c_{012\alpha} - u'_{1e} s_{012\alpha}) - u_{2e}(u'_{1e} c_{012\alpha} + s_{012\alpha}) \\ L_2(s_{012\alpha} + u'_{1e} c_{012\alpha}) + u_{2e}(-u'_{1e} s_{012\alpha} + c_{012\alpha}) \end{bmatrix}, \end{aligned} \tag{7}$$

where $c_{0\alpha} = \cos(\theta_0 + \alpha)$, $s_{0\alpha} = \sin(\theta_0 + \alpha)$, $c_{01\alpha} = \cos(\theta_0 + \theta_1 + \alpha)$, $s_{01\alpha} = \sin(\theta_0 + \theta_1 + \alpha)$, $c_{012\alpha} = \cos(\theta_0 + \theta_1 + \theta_2 + \alpha)$, $s_{012\alpha} = \sin(\theta_0 + \theta_1 + \theta_2 + \alpha)$.

The differentiation of (3)–(7) gives the velocities of the system, and are required to derive the kinetic equations of the SRFM.

3.2. Assumed Mode Method

In this method, the elastic displacements of the flexible links are defined by a reduced finite modal series with respect to spatial mode eigen functions and amplitudes with time-varying mode [9,49]. The deflections of the flexible links can be written as,

$$\boldsymbol{u}_i(x_{fi}, t) = \sum_{j=1}^{N_i} \psi_{ij}(x_{fi}).\delta_{ij}(t), \tag{8}$$

where $\psi_{ij}(x_{fi})$ denotes the vector of mode shape functions and $\delta_{ij}(t)$ represents the vector of time-varying generalized coordinates of the i flexible link with j assumed mode and N_i the number of modes of flexible deflection. The model accuracy can be improved by increasing the number of modes. However, the high-order model creates complexity in controller design. According to Fan [10], typically N_i is assumed to be 1 or 2. The mode shape functions are affected by the boundary conditions, physical parameters of the systems, the payload, and the structures of the system. Hence, the proper selection of the boundary conditions is important because it significantly influences the results as mentioned in [31]. Now, the assumed mode shape functions for cantilever beam can be written as in [51],

$$\begin{aligned} \psi_{ij}(x_{fi}) = & \cosh\left(\frac{\beta_j x_{Li}}{L_i}\right) - \cos\left(\frac{\beta_j x_{Li}}{L_i}\right) \\ & - \gamma_j \left[\sinh\left(\frac{\beta_j x_{Li}}{L_i}\right) - \sin\left(\frac{\beta_j x_{Li}}{L_i}\right)\right], \end{aligned} \tag{9}$$

where

$$\gamma_j = \frac{\cosh(\beta_j) + \cos(\beta_j)}{\sinh(\beta_j) + \sin(\beta_j)}, \tag{10}$$

and β_j is solved from the relation $1 + \cosh(\beta_j)\cos(\beta_j) = 0$.

3.3. Kinetic and potential energy of space robot with flexible manipulator

The total kinetic energy of the SRFM is the sum of the kinetic energy of rigid spacecraft base, link 1, rigid hub, link 2, and rigid end-point payload and is given by,

$$K.E_S = K.E_b + K.E_{P1} + K.E_H + K.E_{P2} + K.E_E, \tag{11}$$

where

$$K.E_b = \frac{1}{2} m_b \dot{r}_b{}^T \dot{r}_b + \frac{1}{2} I_b \dot{\theta}_0{}^2, \tag{12}$$

$$K.E_{P1} = \frac{1}{2} \int_0^{L_1} \rho_1 \dot{r}_{P1}^T \dot{r}_{P1} dx_{L1}, \tag{13}$$

$$K.E_H = \frac{1}{2} m_H \dot{r}_H^T \dot{r}_H + \frac{1}{2} I_H \left(\dot{\theta}_0 + \dot{\theta}_1 + \dot{u}'_{1e}\right)^2, \tag{14}$$

$$K.E_{P2} = \frac{1}{2} \int_0^{L_2} \rho_2 \dot{r}_{P2}^T \dot{r}_{P2} dx_{L2}, \tag{15}$$

$$K.E_E = \frac{1}{2} m_E \dot{r}_E^T \dot{r}_E + \frac{1}{2} I_E \left(\dot{\theta}_0 + \dot{\theta}_1 + \dot{\theta}_2 + \dot{u}'_{1e} + \dot{u}'_{2e}\right)^2, \tag{16}$$

The potential energy of the system is due to the elastic deformation of robot arms only and is given by,

$$P.E_S = \sum_{i=1}^{2} \frac{1}{2} \int_0^{L_i} (EI)_i \left(u''_i\right)^2 dx_{Li}, \tag{17}$$

where $u''_i = \dfrac{\partial^2 u_i}{\partial x_{Li}^2}$.

3.4. Pre-impact dynamics model of space robot with flexible manipulator

The dynamic equation of the SRFM is obtained by using the Lagrangian equation as,

$$\frac{d}{dt}\left[\frac{\partial L_S}{\partial \dot{\boldsymbol{q}}_t}\right] - \frac{\partial L_S}{\partial \boldsymbol{q}_t} = \boldsymbol{\tau}_t, \tag{18}$$

where $\boldsymbol{q}_t = [\boldsymbol{q}_R, \boldsymbol{q}_F]^T = \left[x_b, y_b, \theta_0, \theta_1, \theta_2, \delta_{11}, \cdots, \delta_{1N_i}, \delta_{21}, \cdots, \delta_{2N_i}\right]^T$ is the generalized coordinate vector of the system, $L_S = K.E_S - P.E_S$ is the Lagrange function of SRFM, $\boldsymbol{\tau}_t = [\boldsymbol{\tau}_R, \boldsymbol{\tau}_F]^T = \left[F_x, F_y, \tau_b, \tau_1, \tau_2, \boldsymbol{0}_{1\times N_i}, \boldsymbol{0}_{1\times N_i}\right]^T$ is the vector of generalized applied input forces/torques.

After derivation, the dynamic equations for the SRFM can be written as,

$$\boldsymbol{H}(\boldsymbol{q}_s)\ddot{\boldsymbol{q}}_s + \boldsymbol{V}(\boldsymbol{q}_s, \dot{\boldsymbol{q}}_s)\dot{\boldsymbol{q}}_s + \boldsymbol{K}_s \boldsymbol{q}_s = \boldsymbol{\tau}_s + \boldsymbol{d}_s, \tag{19}$$

where $\boldsymbol{H}(\boldsymbol{q}_s)$ represents the generalized inertia matrix of the system, $\boldsymbol{V}(\boldsymbol{q}_s, \dot{\boldsymbol{q}}_s)$ denotes the generalized Coriolis and centrifugal forces matrix, and $\boldsymbol{K}_s$ is the generalized stiffness matrix.

The generalized coordinate vector of the system is denoted by $\boldsymbol{q}_s = [\boldsymbol{q}_R, \boldsymbol{q}_F]^T = \left[x_b, y_b, \theta_0, \theta_1, \theta_2, \delta_{11}, \cdots, \delta_{1N_i}, \delta_{21}, \cdots, \delta_{2N_i}\right]^T$. Here, $[x_b, y_b, \theta_0, \theta_1, \theta_2]^T$ represents the rigid motion of the system. Similarly, $\left[\delta_{11}, \cdots, \delta_{1N_i}, \delta_{21}, \cdots, \delta_{2N_i}\right]^T$ is the generalized coordinate vector of the flexible motion, and $\boldsymbol{d}_s$ denotes the vector of external disturbance forces/torques applied in rigid and flexible motion. Here $\boldsymbol{d}_s = [\boldsymbol{d}_R, \boldsymbol{d}_F]^T = [\boldsymbol{J}_{FJ}\boldsymbol{F}_e, \boldsymbol{0}]^T$, where $\boldsymbol{J}_{FJ}$ is the Jacobian transpose, and $\boldsymbol{F}_e$ denotes the contact force in the $X-Y$ plane. The system dynamic equations given in (19) can also be written in the following form,

$$\begin{bmatrix} \boldsymbol{H}_{RR} & \boldsymbol{H}_{RF} \\ \boldsymbol{H}_{FR} & \boldsymbol{H}_{FF} \end{bmatrix} \begin{bmatrix} \ddot{\boldsymbol{q}}_R \\ \ddot{\boldsymbol{q}}_F \end{bmatrix} + \begin{bmatrix} \boldsymbol{V}_{RR} & \boldsymbol{V}_{RF} \\ \boldsymbol{V}_{FR} & \boldsymbol{V}_{FF} \end{bmatrix} \begin{bmatrix} \dot{\boldsymbol{q}}_R \\ \dot{\boldsymbol{q}}_F \end{bmatrix} + \begin{bmatrix} \boldsymbol{0} \\ \boldsymbol{K}_{FF}\boldsymbol{q}_F \end{bmatrix} = \left[\boldsymbol{\tau}_R + \boldsymbol{d}_R; \boldsymbol{0}\right], \tag{20}$$

where the subscripts R and F represent the rigid and flexible motion of the system, respectively. To track the desired trajectory of the end-effector, the dynamic equation based on joint space is transformed to the task space. The relationship between the motion in the task space vs joint space in terms of $\dot{\boldsymbol{q}}_R$ and $\ddot{\boldsymbol{q}}_R$ is given by

$$\begin{aligned} \dot{\boldsymbol{q}}_R &= \boldsymbol{J}_R^{-1}\left(\dot{\boldsymbol{p}}_s - \boldsymbol{J}_F\dot{\boldsymbol{q}}_F\right), \\ \ddot{\boldsymbol{q}}_R &= \boldsymbol{J}_R^{-1}\ddot{\boldsymbol{p}}_s - \boldsymbol{J}_R^{-1}\boldsymbol{J}_F\ddot{\boldsymbol{q}}_F - \boldsymbol{J}_R^{-1}\dot{\boldsymbol{J}}_R\boldsymbol{J}_R^{-1}\dot{\boldsymbol{p}}_s + \boldsymbol{J}_R^{-1}\left(\dot{\boldsymbol{J}}_R\boldsymbol{J}_R^{-1}\boldsymbol{J}_F - \dot{\boldsymbol{J}}_F\right)\dot{\boldsymbol{q}}_F, \end{aligned} \tag{21}$$

where $\boldsymbol{p}_s = [x_b, y_b, \theta_0, x_{ep}, y_{ep}]^T$ gives the actual rigid motion states in the task space, x_{ep} and y_{ep} are the vectors of the end-effector position, $\boldsymbol{J}_R = \frac{\partial \boldsymbol{p}_s}{\partial \boldsymbol{q}_R}$ and $\boldsymbol{J}_F = \frac{\partial \boldsymbol{p}_s}{\partial \boldsymbol{q}_F}$. Rearranging (21) into (20) gives the final dynamic equations in the task space, which are

$$\boldsymbol{A}_{TRR}\ddot{\boldsymbol{p}}_s + \boldsymbol{A}_{TRF}\ddot{\boldsymbol{q}}_F + \boldsymbol{B}_{TRR}\dot{\boldsymbol{p}}_s + \boldsymbol{B}_{TRF}\dot{\boldsymbol{q}}_F = \boldsymbol{\tau}_R + \boldsymbol{d}_R, \tag{22}$$

$$\boldsymbol{A}_{TFR}\ddot{\boldsymbol{p}}_s + \boldsymbol{A}_{TFF}\ddot{\boldsymbol{q}}_F + \boldsymbol{B}_{TFR}\dot{\boldsymbol{p}}_s + \boldsymbol{B}_{TFF}\dot{\boldsymbol{q}}_F + \boldsymbol{K}_{FF}\boldsymbol{q}_F = \boldsymbol{0}, \tag{23}$$

where the subscript T represents the task space and

$$\begin{aligned} &\boldsymbol{A}_{TRR} = \boldsymbol{H}_{RR}\boldsymbol{J}_R^{-1}, \quad \boldsymbol{A}_{TRF} = -\boldsymbol{H}_{RR}\boldsymbol{J}_R^{-1}\boldsymbol{J}_F + \boldsymbol{H}_{RF}, \\ &\boldsymbol{A}_{TFR} = \boldsymbol{H}_{FR}\boldsymbol{J}_R^{-1}, \quad \boldsymbol{A}_{TFF} = -\boldsymbol{H}_{FR}\boldsymbol{J}_R^{-1}\boldsymbol{J}_F + \boldsymbol{H}_{FF}, \\ &\boldsymbol{B}_{TRR} = -\boldsymbol{H}_{RR}\boldsymbol{J}_R^{-1}\dot{\boldsymbol{J}}_R\boldsymbol{J}_R^{-1} + \boldsymbol{V}_{RR}\boldsymbol{J}_R^{-1}, \\ &\boldsymbol{B}_{TRF} = \boldsymbol{H}_{RR}\boldsymbol{J}_R^{-1}(\dot{\boldsymbol{J}}_R\boldsymbol{J}_R^{-1}\boldsymbol{J}_F - \dot{\boldsymbol{J}}_F) - \boldsymbol{V}_{RR}\boldsymbol{J}_R^{-1}\boldsymbol{J}_F + \boldsymbol{V}_{RF}, \\ &\boldsymbol{B}_{TFR} = -\boldsymbol{H}_{FR}\boldsymbol{J}_R^{-1}\dot{\boldsymbol{J}}_R\boldsymbol{J}_R^{-1} + \boldsymbol{V}_{FR}\boldsymbol{J}_R^{-1}, \\ &\boldsymbol{B}_{TFF} = \boldsymbol{H}_{FR}\boldsymbol{J}_R^{-1}(\dot{\boldsymbol{J}}_R\boldsymbol{J}_R^{-1}\boldsymbol{J}_F - \dot{\boldsymbol{J}}_F) - \boldsymbol{V}_{FR}\boldsymbol{J}_R^{-1}\boldsymbol{J}_F + \boldsymbol{V}_{FF}. \end{aligned}$$

3.5. Initial conditions for post-impact dynamics

The generalized velocities of the system change during the impact period. However, it is assumed that the generalized coordinates of the system remain the same, as in [30]. For simplicity, the final dynamic equations of the space robot with the flexible manipulator in the task space, as shown in (22) and (23), can be written in compact form as,

$$\boldsymbol{A}_T\ddot{\boldsymbol{p}} + \boldsymbol{B}_T\dot{\boldsymbol{p}} + \boldsymbol{K}_s\boldsymbol{p} = \boldsymbol{\tau}_s + \boldsymbol{J}_{FJ}\boldsymbol{F}_e. \tag{24}$$

Similarly, the dynamic equations of the rigid external object are obtained as,

$$\boldsymbol{M}_o\ddot{\boldsymbol{p}}_o + \boldsymbol{C}_o = -\boldsymbol{J}_o^T\boldsymbol{F}_e, \tag{25}$$

where the subscript o represents the object, $\boldsymbol{M}_o$, $\boldsymbol{C}_o$, $\boldsymbol{p}_o$ and $\boldsymbol{J}_o^T$ denote, respectively, the generalized inertia matrix, the vector relating to Coriolis and centrifugal forces, the generalized co-ordinate vector of the object, and the transpose Jacobian matrix of the object. Rearranging (25) in terms of $\boldsymbol{F}_e$ and substitution into (24) provides the following equation:

$$\boldsymbol{A}_T\ddot{\boldsymbol{p}} + \boldsymbol{B}_T\dot{\boldsymbol{p}} + \boldsymbol{K}_s\boldsymbol{p} = \boldsymbol{\tau}_s - \boldsymbol{J}_{FJ}(\boldsymbol{J}_o^T)^{-1}(\boldsymbol{M}_o\ddot{\boldsymbol{p}}_o + \boldsymbol{C}_o). \tag{26}$$

The above Eq. (26) is integrated over the impact period t_I and can be written as,

$$\begin{aligned} \int_0^{t_I} \boldsymbol{A}_T\ddot{\boldsymbol{p}}dt + \int_0^{t_I}\left(\boldsymbol{B}_T\dot{\boldsymbol{p}} + \boldsymbol{K}_s\boldsymbol{p}\right)dt = \\ -\int_0^{t_I}\left(\boldsymbol{J}_{FJ}(\boldsymbol{J}_o^T)^{-1}\boldsymbol{M}_o\ddot{\boldsymbol{p}}_o\right)dt + \int_0^{t_I}\left(\boldsymbol{\tau}_s - \boldsymbol{J}_{FJ}(\boldsymbol{J}_o^T)^{-1}\boldsymbol{C}_o\right)dt. \end{aligned} \tag{27}$$

It is assumed that no control inputs are applied to the system during the impact stage. In addition, the duration of the impact force is short and the magnitude of the impact force is large. Mathematically, it can be expressed as in [30]:

$$t_I = O(\epsilon_p), \quad \ddot{\boldsymbol{p}}, \ddot{\boldsymbol{p}}_o = O\left(\frac{1}{\epsilon_p}\right), \quad \boldsymbol{p}, \dot{\boldsymbol{p}}, \boldsymbol{p}_o, \dot{\boldsymbol{p}}_o = O(1), \quad \epsilon_p << 1. \tag{28}$$

The integration of (27) results in,

$$\begin{aligned} \boldsymbol{A}_T(\dot{\boldsymbol{p}}_a - \dot{\boldsymbol{p}}_b) + \boldsymbol{J}_{FJ}(\boldsymbol{J}_o^T)^{-1}\boldsymbol{M}_o(\dot{\boldsymbol{p}}_{oa} - \dot{\boldsymbol{p}}_{ob}) \\ = \int_0^{t_I}\left(\boldsymbol{\tau}_s - \boldsymbol{J}_{FJ}(\boldsymbol{J}_o^T)^{-1}\boldsymbol{C}_o - \boldsymbol{B}_T\dot{\boldsymbol{p}} - \boldsymbol{K}_s\boldsymbol{p}\right)dt, \end{aligned} \tag{29}$$

where the subscripts a and b represent the quantities after and before the impact, respectively. The left hand side of (29) is $O(1)$ while the function that is to be integrated on the right hand side of (29) is also $O(1)$. Hence, the integration over t_I of (29) is $O(\epsilon_p)$ and can be neglected. Then, (29) can be written as,

$$\boldsymbol{A}_T(\dot{\boldsymbol{p}}_a - \dot{\boldsymbol{p}}_b) + \boldsymbol{J}_{FJ}\left(\boldsymbol{J}_o^T\right)^{-1}\boldsymbol{M}_o(\dot{\boldsymbol{p}}_{oa} - \dot{\boldsymbol{p}}_{ob}) = \boldsymbol{0}. \tag{30}$$

Immediately, after impact, the velocity of the contact point of each system remains the same. Thus, the following relation can be obtained,

$$\boldsymbol{J}_J\dot{\boldsymbol{p}}_a = \boldsymbol{J}_o\dot{\boldsymbol{p}}_{oa}, \tag{31}$$

where $\boldsymbol{J}_J$ is the Jacobian of the space robot system with the flexible manipulator. The generalized velocities of the object can be written in terms of the robotic arm from (31) as,

$$\dot{\boldsymbol{p}}_{oa} = \boldsymbol{J}_o^{-1}\boldsymbol{J}_J\dot{\boldsymbol{p}}_a. \tag{32}$$

Substitution of $\dot{\boldsymbol{p}}_{oa}$ from (32) in (30) gives the impact effect on the space manipulator motion as,

$$\dot{\boldsymbol{p}}_a = \boldsymbol{G}_I^{-1}\boldsymbol{N}_I, \tag{33}$$

where $\boldsymbol{G}_I = \boldsymbol{A}_T + \boldsymbol{J}_{FJ}(\boldsymbol{J}_o^T)^{-1}\boldsymbol{M}_o\boldsymbol{J}_o^T\boldsymbol{J}_J$ and

$\boldsymbol{N}_I = \boldsymbol{A}_T\dot{\boldsymbol{p}}_b + \boldsymbol{J}_{FJ}(\boldsymbol{J}_o^T)^{-1}\boldsymbol{M}_o\dot{\boldsymbol{p}}_{ob}$.

This motion represents the undesirable behavior of the space robot manipulator system after impact with an external object.

3.6. Post-impact dynamics of combined space robot with flexible manipulator and object

After the impact of the flexible space robot with an object, the velocities of the end-effector of the robot will be equal to those of the object. Therefore, the post-impact dynamic model will contain both the space robot with flexible manipulator subsystem and the object subsystem. Hence, the following relation can be written,

$$\boldsymbol{J}_J\dot{\boldsymbol{p}} = \boldsymbol{J}_o\dot{\boldsymbol{p}}_o \Longrightarrow \boldsymbol{J}_J\dot{\boldsymbol{p}} - \boldsymbol{J}_o\dot{\boldsymbol{p}}_o = 0. \tag{34}$$

Differentiating (34) yields,

$$\ddot{\boldsymbol{p}}_o = \boldsymbol{J}_o^{-1}\boldsymbol{J}_J\ddot{\boldsymbol{p}} + \boldsymbol{J}_o^{-1}\left(\dot{\boldsymbol{J}}_J - \dot{\boldsymbol{J}}_o\boldsymbol{J}_o^{-1}\boldsymbol{J}_J\right)\dot{\boldsymbol{p}}. \tag{35}$$

Substitution of (35) in (25) gives,

$$\boldsymbol{M}_o\boldsymbol{J}_o^{-1}\boldsymbol{J}_J\ddot{\boldsymbol{p}} + \boldsymbol{M}_o\boldsymbol{J}_o^{-1}\left(\dot{\boldsymbol{J}}_J - \dot{\boldsymbol{J}}_o\boldsymbol{J}_o^{-1}\boldsymbol{J}_J\right)\dot{\boldsymbol{p}} + \boldsymbol{C}_o = -\boldsymbol{J}_o^T\boldsymbol{F}_e. \tag{36}$$

Again, substitution of (36) in (26) yields,

$$\boldsymbol{A}_T\ddot{\boldsymbol{p}}+\boldsymbol{B}_T\dot{\boldsymbol{p}}+\boldsymbol{K}_s\boldsymbol{p}=\boldsymbol{\tau}_s-\boldsymbol{J}_{FJ}(\boldsymbol{J}_o^T)^{-1}\left(\boldsymbol{M}_o\boldsymbol{J}_o^{-1}\boldsymbol{J}_J\dot{\boldsymbol{p}}\right)-\boldsymbol{J}_{FJ}\left(\boldsymbol{J}_o^T\right)^{-1}\boldsymbol{M}_o\boldsymbol{J}_o^{-1}\left(\dot{\boldsymbol{J}}_J-\dot{\boldsymbol{J}}_o\boldsymbol{J}_o^{-1}\boldsymbol{J}_J\right)\dot{\boldsymbol{p}}-\boldsymbol{J}_{FJ}(\boldsymbol{J}_o^T)^{-1}\boldsymbol{C}_o. \tag{37}$$

For simplicity, (37) can be written as,

$$\boldsymbol{M}^*\ddot{\boldsymbol{p}}+\boldsymbol{C}^*\dot{\boldsymbol{p}}+\boldsymbol{K}_s\boldsymbol{p}=\boldsymbol{\tau}_s, \tag{38}$$

where $\boldsymbol{M}^*=\boldsymbol{A}_T+\boldsymbol{J}_{FJ}(\boldsymbol{J}_o^T)^{-1}\boldsymbol{M}_o\boldsymbol{J}_o^{-1}\boldsymbol{J}_J$ and $\boldsymbol{C}^*\dot{\boldsymbol{p}}=\boldsymbol{J}_{FJ}(\boldsymbol{J}_o^T)^{-1}\boldsymbol{M}_o\boldsymbol{J}_o^{-1}(\dot{\boldsymbol{J}}_J-\dot{\boldsymbol{J}}_o\boldsymbol{J}_o^{-1}\boldsymbol{J}_J)\dot{\boldsymbol{p}}-\boldsymbol{J}_{FJ}(\boldsymbol{J}_o^T)^{-1}\boldsymbol{C}_o+\boldsymbol{B}_T\dot{\boldsymbol{p}}$, where $\boldsymbol{M}^*$ and $\boldsymbol{C}^*$ represent the generalized mass matrix, and the Coriolis and centrifugal terms of the post-impact dynamic model of the combined space robot with flexible manipulator and the object, respectively.

4. Singular perturbation model

A singular perturbed model for flexible space manipulators based on joint angles has been proposed in [51,56]. In this paper, the same technique is used to develop the control law using singular perturbed model of SRFM but, based on task space. The main principle of a single perturbation method is to separate the dynamic equations of the system into rigid motion and flexible motion as slow subsystem and fast subsystem, respectively. The post-impact dynamic equations of the system, given in (38), can be written in the following form:

$$\begin{bmatrix}\boldsymbol{M}^*_{RR} & \boldsymbol{M}^*_{RF}\\ \boldsymbol{M}^*_{FR} & \boldsymbol{M}^*_{FF}\end{bmatrix}\begin{bmatrix}\ddot{\boldsymbol{p}}_s\\ \ddot{\boldsymbol{q}}_F\end{bmatrix}+\begin{bmatrix}\boldsymbol{C}^*_{RR} & \boldsymbol{C}^*_{RF}\\ \boldsymbol{C}^*_{FR} & \boldsymbol{C}^*_{FF}\end{bmatrix}\begin{bmatrix}\dot{\boldsymbol{p}}_s\\ \dot{\boldsymbol{q}}_F\end{bmatrix}+\begin{bmatrix}\boldsymbol{0}\\ \boldsymbol{K}_{FF}\boldsymbol{q}_F\end{bmatrix}=\begin{bmatrix}\boldsymbol{\tau}_R\\ \boldsymbol{0}\end{bmatrix}. \tag{39}$$

The above matrix form of (39) can be reformulated as,

$$\begin{bmatrix}\ddot{\boldsymbol{p}}_s\\ \ddot{\boldsymbol{q}}_F\end{bmatrix}=\begin{bmatrix}\boldsymbol{M}^*_{RR} & \boldsymbol{M}^*_{RF}\\ \boldsymbol{M}^*_{FR} & \boldsymbol{M}^*_{FF}\end{bmatrix}^{-1}\begin{bmatrix}\boldsymbol{\tau}_R\\ \boldsymbol{0}\end{bmatrix}-\begin{bmatrix}\boldsymbol{M}^*_{RR} & \boldsymbol{M}^*_{RF}\\ \boldsymbol{M}^*_{FR} & \boldsymbol{M}^*_{FF}\end{bmatrix}^{-1}\begin{bmatrix}\boldsymbol{0}\\ \boldsymbol{K}_{FF}\boldsymbol{q}_F\end{bmatrix}-\begin{bmatrix}\boldsymbol{M}^*_{RR} & \boldsymbol{M}^*_{RF}\\ \boldsymbol{M}^*_{FR} & \boldsymbol{M}^*_{FF}\end{bmatrix}^{-1}\begin{bmatrix}\boldsymbol{C}^*_{RR} & \boldsymbol{C}^*_{RF}\\ \boldsymbol{C}^*_{FR} & \boldsymbol{C}^*_{FF}\end{bmatrix}\begin{bmatrix}\dot{\boldsymbol{p}}_s\\ \dot{\boldsymbol{q}}_F\end{bmatrix}. \tag{40}$$

As the inertial matrix $\boldsymbol{M}^*$ is positive definite, we denote $\boldsymbol{M}^{*-1}$ by $\boldsymbol{W}^*$ and rewrite as follows:

$$\boldsymbol{W}^*=\boldsymbol{M}^{*-1}=\begin{bmatrix}\boldsymbol{M}^*_{RR} & \boldsymbol{M}^*_{RF}\\ \boldsymbol{M}^*_{FR} & \boldsymbol{M}^*_{FF}\end{bmatrix}^{-1}=\begin{bmatrix}\boldsymbol{W}^*_{RR} & \boldsymbol{W}^*_{RF}\\ \boldsymbol{W}^*_{FR} & \boldsymbol{W}^*_{FF}\end{bmatrix}, \tag{41}$$

where

$$\begin{aligned}\boldsymbol{W}^*_{RR}&=\left(\boldsymbol{M}^*_{RR}-\boldsymbol{M}^*_{RF}\boldsymbol{M}^{*-1}_{FF}\boldsymbol{M}^*_{FR}\right)^{-1},\\ \boldsymbol{W}^*_{RF}&=-\boldsymbol{M}^{*-1}_{RR}\boldsymbol{M}^*_{RF}\left(\boldsymbol{M}^*_{FF}-\boldsymbol{M}^*_{FR}\boldsymbol{M}^{*-1}_{RR}\boldsymbol{M}^*_{RF}\right)^{-1},\\ \boldsymbol{W}^*_{FR}&=-\boldsymbol{M}^{*-1}_{FF}\boldsymbol{M}^*_{FR}\left(\boldsymbol{M}^*_{RR}-\boldsymbol{M}^*_{RF}\boldsymbol{M}^{*-1}_{FF}\boldsymbol{M}^*_{FR}\right)^{-1},\\ \boldsymbol{W}^*_{FF}&=\left(\boldsymbol{M}^*_{FF}-\boldsymbol{M}^*_{FR}\boldsymbol{M}^{*-1}_{RR}\boldsymbol{M}^*_{RF}\right)^{-1}.\end{aligned} \tag{42}$$

Using (41) and (42), the matrix form of (40) can be written into the following two separate equations in rigid and flexible part individually:

$$\begin{aligned}\ddot{p}_s=&-\boldsymbol{W}^*_{RF}(\boldsymbol{p}_s,\boldsymbol{q}_F)\boldsymbol{K}_{FF}\boldsymbol{q}_F+\boldsymbol{W}^*_{RR}(\boldsymbol{p}_s,\boldsymbol{q}_F)\boldsymbol{\tau}_R\\ &-\left(\boldsymbol{W}^*_{RR}(\boldsymbol{p}_s,\boldsymbol{q}_F)\boldsymbol{C}^*_{RR}\left(\boldsymbol{p}_s,\dot{p}_s,\boldsymbol{q}_F,\dot{\boldsymbol{q}}_F\right)\right.\\ &\left.+\boldsymbol{W}^*_{RF}(\boldsymbol{p}_s,\boldsymbol{q}_F)\boldsymbol{C}^*_{FR}\left(\boldsymbol{p}_s,\dot{\boldsymbol{p}}_s,\boldsymbol{q}_F,\dot{\boldsymbol{q}}_F\right)\right)\dot{\boldsymbol{p}}_s\\ &-\left(\boldsymbol{W}^*_{RR}(\boldsymbol{p}_s,\boldsymbol{q}_F)\boldsymbol{C}^*_{RF}\left(\boldsymbol{p}_s,\dot{\boldsymbol{p}}_s,\boldsymbol{q}_F,\dot{q}_F\right)\right.\\ &\left.+\boldsymbol{W}^*_{RF}(\boldsymbol{p}_s,\boldsymbol{q}_F)\boldsymbol{C}^*_{FF}\left(\boldsymbol{p}_s,\dot{p}_s,\boldsymbol{q}_F,\dot{\boldsymbol{q}}_F\right)\dot{\boldsymbol{q}}_F,\right.\end{aligned} \tag{43}$$

$$\begin{aligned}\ddot{\boldsymbol{q}}_F=&-\boldsymbol{W}^*_{FF}(\boldsymbol{p}_s,\boldsymbol{q}_F)\boldsymbol{K}_{FF}\boldsymbol{q}_F+\boldsymbol{W}^*_{FR}(\boldsymbol{p}_s,\boldsymbol{q}_F)\boldsymbol{\tau}_R\\ &-\left(\boldsymbol{W}^*_{FR}(\boldsymbol{p}_s,\boldsymbol{q}_F)\boldsymbol{C}^*_{RR}\left(\boldsymbol{p}_s,\dot{\boldsymbol{p}}_s,\boldsymbol{q}_F,\dot{\boldsymbol{q}}_F\right)\right.\\ &\left.+\boldsymbol{W}^*_{FF}(\boldsymbol{p}_s,\boldsymbol{q}_F)\boldsymbol{C}^*_{FR}\left(\boldsymbol{p}_s,\dot{\boldsymbol{p}}_s,\boldsymbol{q}_F,\dot{\boldsymbol{q}}_F\right)\dot{\boldsymbol{p}}_s\right.\\ &-\left(\boldsymbol{W}^*_{FR}(\boldsymbol{p}_s,\boldsymbol{q}_F)\boldsymbol{C}^*_{RF}\left(\boldsymbol{p}_s,\dot{\boldsymbol{p}}_s,\boldsymbol{q}_F,\dot{\boldsymbol{q}}_F\right)\right.\\ &\left.+\boldsymbol{W}^*_{FF}(\boldsymbol{p}_s,\boldsymbol{q}_F)\boldsymbol{C}^*_{FF}\left(\boldsymbol{p}_s,\dot{\boldsymbol{p}}_s,\boldsymbol{q}_F,\dot{\boldsymbol{q}}_F\right)\right)\dot{\boldsymbol{q}}_F.\end{aligned} \tag{44}$$

Referring to [56], assuming k_m is the smallest element of the flexible link stiffness matrix $\boldsymbol{K}_{FF}$, the new variable $\varepsilon^2=1/k_m$ is defined. If k_m is very large, $\varepsilon\to 0$. Then, the new variables $\boldsymbol{\xi}=\boldsymbol{q}_F/\varepsilon^2$ and $\tilde{\boldsymbol{K}}_{FF}=\varepsilon^2\boldsymbol{K}_{FF}$ are defined. Substitution of $\boldsymbol{q}_F=\varepsilon^2\boldsymbol{\xi}$ and $\boldsymbol{K}_{FF}=\tilde{\boldsymbol{K}}_{FF}/\varepsilon^2$ in (43) and (44) yields the dynamic equations of SRFM in singular perturbation form as,

$$\begin{aligned}\ddot{\boldsymbol{p}}_s=&\boldsymbol{W}^*_{RR}(\boldsymbol{p}_s,\varepsilon^2\boldsymbol{\xi})\boldsymbol{\tau}_R-\boldsymbol{W}^*_{RF}(\boldsymbol{p}_s,\varepsilon^2\boldsymbol{\xi})\tilde{\boldsymbol{K}}_{FF}\boldsymbol{\xi}\\ &-\left(\boldsymbol{W}^*_{RR}(\boldsymbol{p}_s,\varepsilon^2\boldsymbol{\xi})\boldsymbol{C}^*_{RR}(\boldsymbol{p}_s,\dot{\boldsymbol{p}}_s,\varepsilon^2\boldsymbol{\xi},\varepsilon^2\dot{\boldsymbol{\xi}})\right.\\ &\left.+\boldsymbol{W}^*_{RF}(\boldsymbol{p}_s,\varepsilon^2\boldsymbol{\xi})\boldsymbol{C}^*_{FR}(\boldsymbol{p}_s,\dot{\boldsymbol{p}}_s,\varepsilon^2\boldsymbol{\xi},\varepsilon^2\dot{\boldsymbol{\xi}})\right)\dot{\boldsymbol{p}}_s\\ &-\left(\boldsymbol{W}^*_{RR}(\boldsymbol{p}_s,\varepsilon^2\boldsymbol{\xi})\boldsymbol{C}^*_{RF}(\boldsymbol{p}_s,\dot{\boldsymbol{p}}_s,\varepsilon^2\boldsymbol{\xi},\varepsilon^2\dot{\boldsymbol{\xi}})\right.\\ &\left.+\boldsymbol{W}^*_{RF}(\boldsymbol{p}_s,\varepsilon^2\boldsymbol{\xi})\boldsymbol{C}^*_{FF}(\boldsymbol{p}_s,\dot{\boldsymbol{p}}_s,\varepsilon^2\boldsymbol{\xi},\varepsilon^2\dot{\boldsymbol{\xi}})\right)\varepsilon^2\dot{\boldsymbol{\xi}}.\end{aligned} \tag{45}$$

$$\begin{aligned}\varepsilon^2\ddot{\boldsymbol{\xi}}=&\boldsymbol{W}^*_{FR}(\boldsymbol{p}_s,\varepsilon^2\boldsymbol{\xi})\boldsymbol{\tau}_R-\boldsymbol{W}^*_{FF}(\boldsymbol{p}_s,\varepsilon^2\boldsymbol{\xi})\tilde{\boldsymbol{K}}_{FF}\boldsymbol{\xi}\\ &-\left(\boldsymbol{W}^*_{FR}(\boldsymbol{p}_s,\varepsilon^2\boldsymbol{\xi})\boldsymbol{C}^*_{RR}(\boldsymbol{p}_s,\dot{\boldsymbol{p}}_s,\varepsilon^2\boldsymbol{\xi},\varepsilon^2\dot{\boldsymbol{\xi}})\right.\\ &\left.+\boldsymbol{W}^*_{FF}(\boldsymbol{p}_s,\varepsilon^2\boldsymbol{\xi})\boldsymbol{C}^*_{FR}(\boldsymbol{p}_s,\dot{\boldsymbol{p}}_s,\varepsilon^2\boldsymbol{\xi},\varepsilon^2\dot{\boldsymbol{\xi}})\right)\dot{\boldsymbol{p}}_s\\ &-\left(\boldsymbol{W}^*_{FR}(\boldsymbol{p}_s,\varepsilon^2\boldsymbol{\xi})\boldsymbol{W}^*_{RF}(\boldsymbol{p}_s,\dot{\boldsymbol{p}}_s,\varepsilon^2\boldsymbol{\xi},\varepsilon^2\dot{\boldsymbol{\xi}})\right.\\ &\left.+\boldsymbol{W}^*_{FF}(\boldsymbol{p}_s,\varepsilon^2\boldsymbol{\xi})\boldsymbol{C}^*_{FF}(\boldsymbol{p}_s,\dot{\boldsymbol{p}}_s,\varepsilon^2\boldsymbol{\xi},\varepsilon^2\dot{\boldsymbol{\xi}})\right)\varepsilon^2\dot{\boldsymbol{\xi}}.\end{aligned} \tag{46}$$

Here, (45) and (46) are in terms of $\varepsilon^2\boldsymbol{\xi}$, and are the singularly perturbed model of SRFM.

4.1. Slow subsystem

The rigid motion of the SRFM is derived from (45) and (46) by setting ε to zero. The following equations are obtained:

$$\ddot{\bar{\boldsymbol{p}}}_s=\bar{\boldsymbol{W}}^*_{RR}\bar{\boldsymbol{\tau}}_R-\bar{\boldsymbol{W}}^*_{RF}\tilde{\boldsymbol{K}}_{FF}\bar{\boldsymbol{\xi}}-\left(\bar{\boldsymbol{W}}^*_{RR}\bar{\boldsymbol{C}}^*_{RR}+\bar{\boldsymbol{W}}^*_{RF}\bar{\boldsymbol{C}}^*_{FR}\right)\dot{\bar{\boldsymbol{p}}}_s, \tag{47}$$

$$\boldsymbol{0}=\bar{\boldsymbol{W}}^*_{FR}\bar{\boldsymbol{\tau}}_R-\bar{\boldsymbol{W}}^*_{FF}\tilde{\boldsymbol{K}}_{FF}\bar{\boldsymbol{\xi}}-\left(\bar{\boldsymbol{W}}^*_{FR}\bar{\boldsymbol{C}}^*_{RR}+\bar{\boldsymbol{W}}^*_{FF}\bar{\boldsymbol{C}}^*_{FR}\right)\dot{\bar{\boldsymbol{p}}}_s. \tag{48}$$

The over bars denote the system with $\varepsilon=0$. From (48), $\bar{\boldsymbol{\xi}}$ is obtained as,

$$\bar{\boldsymbol{\xi}}=\bar{\boldsymbol{W}}^{*-1}_{FF}\tilde{\boldsymbol{K}}^{-1}_{FF}\left(\bar{\boldsymbol{W}}^*_{FR}\bar{\boldsymbol{\tau}}_R-\left(\bar{\boldsymbol{W}}^*_{FR}\bar{\boldsymbol{C}}^*_{RR}+\bar{\boldsymbol{W}}^*_{FF}\bar{\boldsymbol{C}}^*_{FR}\right)\dot{\bar{\boldsymbol{p}}}_s\right). \tag{49}$$

Substitution of (49) into (43) and using (41) gives the rigid body dynamics of SRFM as follows,

$$\bar{\boldsymbol{M}}^*_{RR}\ddot{\bar{\boldsymbol{p}}}_s+\bar{\boldsymbol{C}}^*_{RR}\dot{\bar{\boldsymbol{p}}}_s=\bar{\boldsymbol{\tau}}_R. \tag{50}$$

Now, the above (50) looks similar to a general space robot system with rigid manipulator provided in the literature. Using (50), a new error state vector $\boldsymbol{e}_n=[\boldsymbol{e}_{n1},\boldsymbol{e}_{n2}]^T$ is introduced where $\boldsymbol{e}_{n1}=\bar{\boldsymbol{p}}_s-\bar{\boldsymbol{p}}_d$, $\boldsymbol{e}_{n2}=\dot{\bar{\boldsymbol{p}}}_s-\dot{\bar{\boldsymbol{p}}}_d$ and $\bar{\boldsymbol{p}}_d$ is the desired rigid motion vector of the system. Rearranging Eq. (50) in terms of error state, gives

$$\dot{\boldsymbol{e}}_{n1}=\boldsymbol{e}_{n2}, \tag{51}$$

$$\dot{\boldsymbol{e}}_{n2}=-\bar{\boldsymbol{M}}^{*-1}_{RR}\bar{\boldsymbol{C}}^*_{RR}\left(\boldsymbol{e}_{n2}+\dot{\bar{\boldsymbol{p}}}_d\right)-\ddot{\bar{\boldsymbol{p}}}_d+\bar{\boldsymbol{M}}^{*-1}_{RR}\bar{\boldsymbol{\tau}}_R. \tag{52}$$

4.2. Fast subsystem

Define the new variables $\boldsymbol{fs}_1 = \boldsymbol{\xi} - \bar{\boldsymbol{\xi}}$ and $\boldsymbol{fs}_2 = \varepsilon\dot{\boldsymbol{\xi}}$. The fast subsystem is derived by defining a fast scale $t_f = \frac{t}{\varepsilon}$. Using these relations, the following expressions can be obtained,

$$\frac{d\boldsymbol{fs}_1}{dt_f} = \boldsymbol{fs}_2 - \varepsilon\dot{\bar{\boldsymbol{\xi}}}, \tag{53}$$

$$\frac{d\boldsymbol{fs}_2}{dt_f} = \varepsilon^2\ddot{\boldsymbol{\xi}}. \tag{54}$$

Substitution of (46) in (54) and again by substituting $\boldsymbol{\xi} = \boldsymbol{fs}_1 + \bar{\boldsymbol{\xi}}$ and $\varepsilon\dot{\boldsymbol{\xi}} = \boldsymbol{fs}_2$ yields,

$$\begin{aligned}\frac{d\boldsymbol{fs}_2}{dt_f} &= \boldsymbol{W}^*_{FR}\boldsymbol{\tau}_R - \boldsymbol{W}^*_{FF}\tilde{\boldsymbol{K}}_{FF}\left(\boldsymbol{fs}_1 + \bar{\boldsymbol{\xi}}\right) - (\boldsymbol{W}^*_{FR}\boldsymbol{C}^*_{RR} + \boldsymbol{W}^*_{FF}\boldsymbol{C}^*_{FR})\dot{\boldsymbol{p}}_s \\ &\quad -(\boldsymbol{W}^*_{FR}\boldsymbol{C}^*_{RF} + \boldsymbol{W}^*_{FF}\boldsymbol{C}^*_{FF})\varepsilon\boldsymbol{fs}_2.\end{aligned} \tag{55}$$

Now, setting $\varepsilon = 0$ in (53) gives,

$$\frac{d\boldsymbol{fs}_1}{dt_f} = \boldsymbol{fs}_2. \tag{56}$$

Similarly, using (49) and setting $\varepsilon = 0$ in (55) obtains,

$$\frac{d\boldsymbol{fs}_2}{dt_f} = \bar{\boldsymbol{W}}^*_{FR}(\boldsymbol{\tau}_R - \bar{\boldsymbol{\tau}}_R) - \bar{\boldsymbol{W}}^*_{FF}\tilde{\boldsymbol{K}}_{FF}\boldsymbol{fs}_1. \tag{57}$$

Then, the following expression can be written from Eqs. (56) and (57) as,

$$\frac{d\boldsymbol{fs}}{dt_f} = \boldsymbol{A}_{FS}\boldsymbol{fs} + \boldsymbol{B}_{FS}\boldsymbol{\tau}_{FS}, \tag{58}$$

where $\boldsymbol{fs} = [\boldsymbol{fs}_1, \boldsymbol{fs}_2]^T$, $\boldsymbol{\tau}_{FS} = \boldsymbol{\tau}_R - \bar{\boldsymbol{\tau}}_R$, $\boldsymbol{A}_{FS} = \begin{bmatrix} \boldsymbol{0} & \boldsymbol{I} \\ -\bar{\boldsymbol{W}}^*_{FF}\tilde{\boldsymbol{K}}_{FF} & \boldsymbol{0} \end{bmatrix}$, $\boldsymbol{B}_{FS} = \begin{bmatrix} \boldsymbol{0} \\ \bar{\boldsymbol{W}}^*_{FR} \end{bmatrix}$, where $\boldsymbol{I}$ and $\boldsymbol{0}$ are the identity and zero matrices with appropriate dimensions, respectively. The subscript FS denotes the fast subsystem.

5. Control law

The main objective of the controller is to control the motion of the entire system after impact with the object. As shown in the previous section, the rigid and flexible dynamics of the system are separated before deriving the control law. Then, two different controllers namely NMPC and SMC are utilized for rigid motion control, while the LQR control law is used to suppress the vibration of the flexible manipulator.

5.1. NMPC

The rigid motion of the post-impact dynamic system can be regulated using one step ahead NMPC law, as described in [25], since NMPC allows for the direct use of nonlinear dynamic equations for prediction [13]. The NMPC law derived using online optimization causes computation delay that cannot be ignored and also the global solution cannot be guaranteed in each optimization problem. Therefore, to minimize the computation burden, NMPC law is derived offline using quadratic performance index of the predictive tracking error and the predictive control inputs. It also guarantees asymptotic tracking of smooth trajectories [16]. The overall control scheme of MPC includes three main ideas. Firstly, an explicit model is used to predict the output of the system at a future time horizon $(t + T_s)$ where T_s is the time increment. After that, the control input is obtained by minimizing the cost function. Then, a receding horizon technique is used, that is at each instant only the first control input is sent to the system and the horizon moves towards the future [19]. The stability proof of the NMPC method for nonlinear system is given in [16,32].

According to Hedjar and Boucher [16], a simple and effective way of predicting the cost function is by expanding the predicting tracking error using Taylor series. Hence, before deriving the control law, the equations of the predicted output and the desired trajectory of the system are expanded on by using a second-order Taylor series as follows:

$$\begin{aligned}\bar{\boldsymbol{p}}_s(t + T_s) &= \bar{\boldsymbol{p}}_s(t) + T_s\dot{\bar{\boldsymbol{p}}}_s(t) + \frac{T_s^2}{2}\ddot{\bar{\boldsymbol{p}}}_S(t), \\ \bar{\boldsymbol{p}}_d(t + T_s) &= \bar{\boldsymbol{p}}_d(t) + T_s\dot{\bar{\boldsymbol{p}}}_d(t) + \frac{T_s^2}{2}\ddot{\bar{\boldsymbol{p}}}_d(t).\end{aligned} \tag{59}$$

where T_s is the predicted tracking horizon. Using (59), the tracking error at time $(t + T_s)$ is derived as,

$$\boldsymbol{e}_{n1}(t + T_s) = \bar{\boldsymbol{p}}_s(t + T_s) - \bar{\boldsymbol{p}}_d(t + T_s). \tag{60}$$

Substituting the expression of $\ddot{\bar{\boldsymbol{p}}}_s$ by rearranging (50) and (59) gives the expression of the tracking error $\boldsymbol{e}_{n1}(t + T_s)$ as,

$$\begin{aligned}\boldsymbol{e}_{n1}(t + T_s) &= \boldsymbol{e}_{n1}(t) + T_s\dot{\boldsymbol{e}}_{n1}(t) + \frac{T_s^2}{2}\bar{\boldsymbol{M}}^{*-1}_{RR}\bar{\boldsymbol{\tau}}_R(t) \\ &\quad -\frac{T_s^2}{2}\bar{\boldsymbol{M}}^{*-1}_{RR}\bar{\boldsymbol{C}}^*_{RR}\dot{\bar{\boldsymbol{p}}}_d(t) - \frac{T_s^2}{2}\ddot{\bar{\boldsymbol{p}}}_d(t).\end{aligned} \tag{61}$$

The next step is to find the control input, which minimizes the tracking error along a fixed time horizon. Therefore, the output tracking error $\boldsymbol{e}_{n1}(t + T_s)$ is used instead of the state vector $\bar{\boldsymbol{p}}_s(t + T_s)$ in the cost function. The control input is calculated by minimizing the following cost function in terms of $\boldsymbol{e}_{n1}(t + T_s)$. The above relation can be written in terms of optimal problem as follows:

$$\begin{cases} \min_{\bar{\boldsymbol{\tau}}_R} & \boldsymbol{f}(\bar{\boldsymbol{\tau}}_R) & = \boldsymbol{e}_{n1}(t + T_s)^T\boldsymbol{e}_{n1}(t + T_s), \\ s.t & \boldsymbol{c}_i(\bar{\boldsymbol{\tau}}_R) & = -(\bar{\boldsymbol{\tau}}_{Ri})^2 + N_i \geq 0, \qquad (i = 1 \ldots 5) \end{cases} \tag{62}$$

where $\boldsymbol{f}(\bar{\boldsymbol{\tau}}_R)$ is the cost function, $\boldsymbol{c}_i(\bar{\boldsymbol{\tau}}_R)$ is the constraint function, and $N_i \geq 0$ are the constraints of $\bar{\boldsymbol{\tau}}_{Ri}$. The penalty function is obtained by solving the constrained optimal problem to get the unconstrained optimal problem as below:

$$P(\bar{\boldsymbol{\tau}}_R) = \bar{\boldsymbol{\tau}}_R(t)^T\bar{\boldsymbol{\tau}}_R(t), \tag{63}$$

which satisfies the following conditions for the penalizing function:

- $P(\bar{\boldsymbol{\tau}}_R)$ is continuous.
- $P(\bar{\boldsymbol{\tau}}_R) \geq 0$.
- $P(\bar{\boldsymbol{\tau}}_R) = 0$, if and only if $\bar{\boldsymbol{\tau}}_R$ is in the feasible set.

Then, the following new unconstrained cost function is written:

$$\begin{aligned}\boldsymbol{J}_c(\boldsymbol{e}_{n1}, \bar{\boldsymbol{\tau}}_R, t) &= \frac{1}{2}\int_t^{(t+T_s)} \big(\boldsymbol{e}_{n1}(t + T_s)^T\boldsymbol{Q}_p\boldsymbol{e}_{n1}(t + T_s) \\ &\quad +\bar{\boldsymbol{\tau}}_R(t)^T\boldsymbol{R}_p\bar{\boldsymbol{\tau}}_R(t)\big)dt,\end{aligned} \tag{64}$$

where $\boldsymbol{Q}_p$ is the positive definite state weighting matrix and $\boldsymbol{R}_p$ is the positive semi-definite input weighting matrix. As the cost function is a convex function, the minimum of the cost function $\boldsymbol{J}_c$ is obtained by taking the first derivative with respect to control input $\bar{\boldsymbol{\tau}}_R$ and equating it to zero. Subsequently after derivation, the control input applied to the system is obtained as,

$$\begin{aligned}\bar{\boldsymbol{\tau}}_R(t) = -&\left[\left(\frac{T_s^2}{2}\bar{\boldsymbol{M}}^{*-1}_{RR}\right)^T\boldsymbol{Q}_p\frac{T_s^2}{2}\bar{\boldsymbol{M}}^{*-1}_{RR} + \boldsymbol{R}_p\right]^{-1}\left(\frac{T_s^2}{2}\bar{\boldsymbol{M}}^{*-1}_{RR}\right)^T\boldsymbol{Q}_p \\ &\left(\boldsymbol{e}_{n1}(t) + T_s\dot{\boldsymbol{e}}_{n1}(t) - \frac{T_s^2}{2}\bar{\boldsymbol{M}}^{*-1}_{RR}\bar{\boldsymbol{C}}^*_{RR}\dot{\bar{\boldsymbol{p}}}_s(t) - \frac{T_s^2}{2}\ddot{\bar{\boldsymbol{p}}}_d(t)\right).\end{aligned} \tag{65}$$

5.1.1. Stability analysis

This section shows the stability of the rigid part of the SRFM system. It is assumed that $\boldsymbol{Q}_p = q_g \boldsymbol{I}_{(n+1)}$ and $\boldsymbol{R}_p = r_g \boldsymbol{I}_{(n+1)}$. That means, the same penalty is used in all the states where q_g and r_g are scalar values. Substitution of the control inputs from (65) into (52) obtains the following relationship:

$$\begin{aligned}\dot{\boldsymbol{e}}_{n2} = &-\bar{\boldsymbol{M}}_{RR}^{*-1}\bar{\boldsymbol{C}}_{RR}^{*}\dot{\bar{\boldsymbol{p}}}_s - \ddot{\bar{\boldsymbol{p}}}_d - \bar{\boldsymbol{M}}_{RR}^{*-1}\boldsymbol{V}_e\left(\frac{T_s^2}{2}\bar{\boldsymbol{M}}_{RR}^{*-1}\right)^T q_g \boldsymbol{I}_{(n+1)}\boldsymbol{e}_{n1}\\ &-\bar{\boldsymbol{M}}_{RR}^{*-1}\boldsymbol{V}_e\left(\frac{T_s^2}{2}\bar{\boldsymbol{M}}_{RR}^{*-1}\right)^T q_g \boldsymbol{I}_{(n+1)} T_s \dot{\boldsymbol{e}}_{n1}(t)\\ &-\bar{\boldsymbol{M}}_{RR}^{*-1}\boldsymbol{V}_e\left(\frac{T_s^2}{2}\bar{\boldsymbol{M}}_{RR}^{*-1}\right)^T q_g \boldsymbol{I}_{(n+1)}\frac{T_s^2}{2}\left(-\bar{\boldsymbol{M}}_{RR}^{*-1}\bar{\boldsymbol{C}}_{RR}^{*}\dot{\bar{\boldsymbol{p}}}(t) - \ddot{\bar{\boldsymbol{p}}}_d(t)\right),\end{aligned} \tag{66}$$

where $\boldsymbol{V}_e = \left[\left(\frac{T_s^2}{2}\bar{\boldsymbol{M}}_{RR}^{*-1}\right)^T \boldsymbol{Q}_p \frac{T_s^2}{2}\bar{\boldsymbol{M}}_{RR}^{*-1} + \boldsymbol{R}_p\right]^{-1}$.

The compact form of Eqs. (51) and (66) can be written as,

$$\dot{\boldsymbol{e}}_n = \boldsymbol{A}_e \boldsymbol{e}_n + \boldsymbol{B}_e \boldsymbol{c}_e, \tag{67}$$

where $\boldsymbol{A}_e = \begin{bmatrix} \boldsymbol{0} & \boldsymbol{I} \\ -\frac{T_s^2}{2}\bar{\boldsymbol{P}}_e q_g & -\frac{T_s^3}{2}\bar{\boldsymbol{P}}_e q_g \end{bmatrix}$, $\boldsymbol{B}_e = \begin{bmatrix} \boldsymbol{0} \\ \boldsymbol{I} \end{bmatrix}$,

$\boldsymbol{c}_e = \frac{T_s^4}{4}\bar{\boldsymbol{P}}_e q_g \bar{\boldsymbol{M}}_{RR}^{*-1}\bar{\boldsymbol{C}}_{RR}\dot{\bar{\boldsymbol{p}}}_s + \frac{T_s^4}{4}\bar{\boldsymbol{P}}_e q_g \ddot{\bar{\boldsymbol{p}}}_d - \bar{\boldsymbol{M}}_{RR}^{*-1}\bar{\boldsymbol{C}}_{RR}^{*}\dot{\bar{\boldsymbol{p}}}_s - \ddot{\bar{\boldsymbol{p}}}_d$, and

$\bar{\boldsymbol{P}}_e = \bar{\boldsymbol{M}}_{RR}^{*-1}\boldsymbol{V}_e(\bar{\boldsymbol{M}}_{RR}^{*-1})^T$.

Let λ be the eigen values of the matrix $\boldsymbol{A}_e$, then the following relation can be written:

$$|\boldsymbol{A}_e - \lambda \boldsymbol{I}| = \boldsymbol{0}. \tag{68}$$

Substituting the expression of $\boldsymbol{A}_e$, and $\boldsymbol{I}_{(6\times6)}$ in (68) yields the following:

$$\lambda^2 + \frac{T_s^3}{2}\bar{\boldsymbol{P}}_e q_g \lambda + \frac{T_s^2}{2}\bar{\boldsymbol{P}}_e q_g = \boldsymbol{0}. \tag{69}$$

Since both $\bar{\boldsymbol{P}}_e$ and $\bar{\boldsymbol{P}}_e^{-1}$ are symmetric, positive definite matrices, the matrix $\bar{\boldsymbol{P}}_e$ will have positive real eigen values [16]. Let $\bar{\lambda}$ be the eigen value of $\bar{\boldsymbol{P}}_e$. Thus, $\bar{\boldsymbol{P}}_e = \bar{\lambda}\boldsymbol{I}$ and, (69) takes the following form:

$$\lambda^2 + \frac{T_s^3}{2}\bar{\lambda} q_g \lambda + \frac{T_s^2}{2}\bar{\lambda} q_g = \boldsymbol{0}. \tag{70}$$

The solutions of (70) give two values of λ: λ_1 and λ_2. The relationship between λ_1 and λ_2 can be computed as,

$$\lambda_1 + \lambda_2 = -\frac{T_s^3}{2}\bar{\lambda} q_g, \tag{71}$$

$$\lambda_1 \lambda_2 = T_s^2 \bar{\lambda} q_g. \tag{72}$$

As $\bar{\lambda}$ is positive, both λ_1 and λ_2 must be negative. Hence, $\boldsymbol{A}_e$ is a stable matrix as the eigen values of this matrix are negative. As $\boldsymbol{A}_e$ is a stable matrix, then for any symmetric positive definite matrix $\boldsymbol{Q}_a = \boldsymbol{Q}_a{}^T > \boldsymbol{0}$, there exists a symmetric positive definite matrix $\boldsymbol{P}_a = \boldsymbol{P}_a{}^T > \boldsymbol{0}$ that satisfies the Lyapunov equation,

$$\dot{\boldsymbol{P}}_a \boldsymbol{A}_e{}^T \boldsymbol{P}_a + \boldsymbol{P}_a \boldsymbol{A}_e = -\boldsymbol{Q}_a. \tag{73}$$

Theorem 1. *The equilibrium point of the dynamic system stated in (67) is asymptotically stable if*

$$\Upsilon < \frac{\lambda_{\min}(\boldsymbol{Q}_a)\lambda_{\max}(\bar{P}_e)}{2r\lambda_{\max}(P_a)}.$$

If $r = 0$, then the origin is an asymptotically stable equilibrium point. Consider $V(\boldsymbol{e}_n) = \boldsymbol{e}_n^T \boldsymbol{P}_a \boldsymbol{e}_n$ as a Lyapunov function candidate for a system (67). Subsequently, the derivative of the Lyapunov function can be written as,

$$\begin{aligned}\dot{V}(\boldsymbol{e}_n) &= \dot{\boldsymbol{e}}_n{}^T \boldsymbol{P}_a \boldsymbol{e}_n + \boldsymbol{e}_n^T \boldsymbol{P}_a \dot{\boldsymbol{e}}_n,\\ &= \left(\boldsymbol{A}_e{}^T \boldsymbol{e}_n{}^T + \boldsymbol{B}_e^T \boldsymbol{c}_e^T\right)\boldsymbol{P}_a \boldsymbol{e}_n + \boldsymbol{e}_n^T \boldsymbol{P}_a (\boldsymbol{A}_e \boldsymbol{e}_n + \boldsymbol{B}_e \boldsymbol{c}_e),\\ &= \boldsymbol{A}_e{}^T \boldsymbol{P}_a \boldsymbol{e}_n \boldsymbol{e}_n{}^T + \boldsymbol{B}_e^T \boldsymbol{c}_e^T \boldsymbol{P}_a \boldsymbol{e}_n + \boldsymbol{e}_n^T \boldsymbol{e}_n \boldsymbol{P}_a \boldsymbol{A}_e + \boldsymbol{e}_n^T \boldsymbol{P}_a \boldsymbol{B}_e \boldsymbol{c}_e,\\ &= -\boldsymbol{e}_n \boldsymbol{e}_n{}^T \boldsymbol{Q}_a + \boldsymbol{B}_e^T \boldsymbol{c}_e^T \boldsymbol{P}_a \boldsymbol{e}_n + \boldsymbol{e}_n^T \boldsymbol{P}_a \boldsymbol{B}_e \boldsymbol{c}_e\\ &\le -\lambda_{\min}(\boldsymbol{Q}_a)\ ||\boldsymbol{e}_n||^2 + 2||\boldsymbol{e}_n||\ ||\boldsymbol{B}_e||\ ||\boldsymbol{c}_e||\ \lambda_{\max}(\boldsymbol{P}_a).\end{aligned} \tag{74}$$

$\dot{V} \le -\kappa||\boldsymbol{e}_n||^2$ is negative definite if $\kappa > 0$, where

$\kappa = \lambda_{\min}(\boldsymbol{Q}_a) - 2||\boldsymbol{B}_e||\ ||\boldsymbol{c}_e||\ \lambda_{\max}(\boldsymbol{P}_a)/||\boldsymbol{e}_n||$. For any $\Upsilon > 0$, there exists $\upsilon > 0$ such that

$$||\boldsymbol{B}_e \boldsymbol{c}_e|| < \Upsilon||\boldsymbol{e}_n||, \quad \forall ||\boldsymbol{e}_n|| < \upsilon, \tag{75}$$

This ensures that $\dot{V}$ is strictly negative for all $||e_n|| < 0$ if $\Upsilon < \frac{\lambda_{\min}(\boldsymbol{Q}_a)}{2r\lambda_{\max}(P_a)}$. This proves the asymptotic stability of the system.

5.1.2. Robustness

To deal with uncertainties, in the model of rigid system defined in (50), the matrices $\bar{\boldsymbol{M}}_{RR}^{*}$ and $\bar{\boldsymbol{C}}_{RR}^{*}$ are split into a nominal part with subscript O and an uncertain part with Δ. Then, the dynamics of SRFM can be written as follows:

$$\left(\bar{\boldsymbol{M}}_{ORR}^{*} + \Delta\bar{\boldsymbol{M}}_{RR}^{*}\right)\ddot{\bar{\boldsymbol{p}}}_s + \left(\bar{\boldsymbol{C}}_{ORR}^{*} + \Delta\bar{\boldsymbol{C}}_{RR}^{*}\right)\dot{\bar{\boldsymbol{p}}}_s = \bar{\boldsymbol{\tau}}_R, \tag{76}$$

where $\bar{\boldsymbol{M}}_{RR}^{*} = \bar{\boldsymbol{M}}_{ORR}^{*} + \Delta\bar{\boldsymbol{M}}_{RR}^{*}$ and $\bar{\boldsymbol{C}}_{RR}^{*} = \bar{\boldsymbol{C}}_{ORR}^{*} + \Delta\bar{\boldsymbol{C}}_{RR}^{*}$. Only the nominal part of the model is used to derive nonlinear predictive control and is given as,

$$\begin{aligned}\bar{\boldsymbol{\tau}}_R(t) = -&\left[\left(\frac{T_s^2}{2}\bar{\boldsymbol{M}}_{ORR}^{*-1}\right)^T \boldsymbol{Q}_p \frac{T_s^2}{2}\bar{\boldsymbol{M}}_{ORR}^{*-1} + \boldsymbol{R}_p\right]^{-1}\left(\frac{T_s^2}{2}\bar{\boldsymbol{M}}_{ORR}^{*-1}\right)^T \boldsymbol{Q}_p\\ &\left(\boldsymbol{e}_{n1}(t) + T_s \dot{\boldsymbol{e}}_{n1}(t) - \frac{T_s^2}{2}\bar{\boldsymbol{M}}_{ORR}^{*-1}\bar{\boldsymbol{C}}_{ORR}^{*}\dot{\bar{\boldsymbol{p}}}_s(t) - \frac{T_s^2}{2}\ddot{\bar{\boldsymbol{p}}}_d(t)\right).\end{aligned} \tag{77}$$

Setting $\boldsymbol{R}_p = \boldsymbol{0}$ in (77) above gives the following relation:

$$\bar{\boldsymbol{\tau}}_R(t) = -\frac{2}{T_s^2}\bar{\boldsymbol{M}}_{ORR}^{*-1}\left(\boldsymbol{e}_{n1}(t) + T_s \dot{\boldsymbol{e}}_{n1}(t)\right) + \bar{\boldsymbol{C}}_{ORR}^{*}\dot{\bar{\boldsymbol{p}}}_s(t) + \bar{\boldsymbol{M}}_{ORR}^{*}\ddot{\bar{\boldsymbol{p}}}_d(t). \tag{78}$$

Substitution of $\bar{\boldsymbol{\tau}}_R(t)$ from (78) in (52)gives:

$$\begin{aligned}&\dot{\boldsymbol{e}}_{n2}(t) + \frac{2}{T_s^2}\bar{\boldsymbol{M}}_{RR}^{*-1}\bar{\boldsymbol{M}}_{ORR}^{*-1}\left(\boldsymbol{e}_{n1}(t) + T_s \dot{\boldsymbol{e}}_{n1}(t)\right)\\ &\quad = \bar{\boldsymbol{M}}_{RR}^{*-1}\left(\Delta\bar{\boldsymbol{M}}_{RR}^{*}\ddot{\bar{\boldsymbol{p}}}_d(t) + \Delta\bar{\boldsymbol{C}}_{RR}^{*}\dot{\bar{\boldsymbol{p}}}_s(t)\right) = \boldsymbol{v}\left(\bar{\boldsymbol{p}}_s, \dot{\bar{\boldsymbol{p}}}_s, \ddot{\bar{\boldsymbol{p}}}_s, t\right).\end{aligned} \tag{79}$$

The above Eq. (79) in the state space form is written as:

$$\dot{\boldsymbol{e}}_n = \boldsymbol{A}_{ro}\boldsymbol{e}_n + \boldsymbol{B}_{ro}\boldsymbol{v}, \tag{80}$$

where $\boldsymbol{A}_{ro} = \begin{bmatrix} \boldsymbol{0} & \boldsymbol{I} \\ -\frac{2}{T_s^2}\bar{\boldsymbol{M}}_{RR}^{*-1}\bar{\boldsymbol{M}}_{ORR}^{*-1} & -\frac{2}{T_s}\bar{\boldsymbol{M}}_{RR}^{*-1}\bar{\boldsymbol{M}}_{ORR}^{*-1} \end{bmatrix}$, $\boldsymbol{B}_{ro} = \begin{bmatrix} \boldsymbol{0} \\ \boldsymbol{I} \end{bmatrix}$.

The following assumptions are made for all $\boldsymbol{p}_s \in \Re^n$ to estimate the bound of function $\boldsymbol{v}$ as,

$$\begin{aligned}&m_o \le ||\bar{\boldsymbol{M}}_{ORR}^{*}|| \le \bar{m}_o,\ ||\Delta\bar{\boldsymbol{M}}_{RR}^{*}|| \le \bar{m} \le \lambda_{\min}(\bar{\boldsymbol{M}}_{RR}^{*}(\boldsymbol{p}_s)),\\ &\quad ||\Delta\bar{\boldsymbol{C}}_{RR}^{*}|| \le \bar{c},\end{aligned}$$

where m_o, $\bar{m}_o$, $\bar{m}$, $\lambda_{\min}$, $\bar{c}$ are positive scalar values. Also, it is assumed that the desired trajectory for the control object is available as bounded functions of time in terms of $\boldsymbol{p}_d$. This means the following inequalities hold:

$$||\boldsymbol{p}_d(t)|| \le n_0,\ ||\dot{\boldsymbol{p}}_d(t)|| \le n_1,\ \textit{and}\ \ ||\ddot{\boldsymbol{p}}_d(t)|| \le n_2,$$

where n_0, n_1, and n_2 are positive scalars. According to Hedjar and Boucher [16], with these above two assumptions, a bounded continuous vector function $\rho(\boldsymbol{e}_n, \dot{\boldsymbol{e}}_n)$ satisfies the following inequality:

$$||\nu|| \le \rho(\boldsymbol{e}_n, \dot{\boldsymbol{e}}_n) \le \gamma||\boldsymbol{e}_n|| \quad \textit{for all} \quad \boldsymbol{p}_s \in \Re^n,$$

where γ is a positive scalar. As both matrices $\bar{\boldsymbol{M}}_{RR}^{*-1}$ and $\bar{\boldsymbol{M}}_{ORR}^{*-1}$ are positive definitive, the matrix $\boldsymbol{a}_{ro} = \bar{\boldsymbol{M}}_{RR}^{*-1}\bar{\boldsymbol{M}}_{ORR}^{*-1}$ has positive real eigen values. Let $\hat{\lambda}$ be the eigen value of $\boldsymbol{a}_{ro}$, giving $\boldsymbol{a}_{ro} = \hat{\lambda}\boldsymbol{I}$. Again, with $\tilde{\lambda}$ as the eigen value of $\boldsymbol{A}_{ro}$, the following relation can be written,

$$|\boldsymbol{A}_{ro} - \tilde{\lambda}\boldsymbol{I}| = \boldsymbol{0}. \tag{81}$$

We now get the following relation after substituting the expression of $\boldsymbol{A}_{ro}$ in (81),

$$\tilde{\lambda}^2 + \frac{2\boldsymbol{a}_{ro}}{T_s}\tilde{\lambda} + \frac{2\boldsymbol{a}_{ro}}{T_s^2} = \boldsymbol{0}. \tag{82}$$

The solution of (82) has two values of $\tilde{\lambda}$ as, $\tilde{\lambda}_1$ and $\tilde{\lambda}_2$, with following relationship:

$$\tilde{\lambda}_1 + \tilde{\lambda}_2 = -\frac{2\hat{\lambda}}{T_s}, \tag{83}$$

$$\tilde{\lambda}_1\tilde{\lambda}_2 = \frac{2\hat{\lambda}}{T_s^2}. \tag{84}$$

As $\hat{\lambda}$ is positive, both $\tilde{\lambda}_1$ and $\tilde{\lambda}_2$ must be negative. Hence, $\boldsymbol{A}_{ro}$ is a stable matrix as the eigen values of this matrix are negative. As $\boldsymbol{A}_{ro}$ is a stable matrix, then for any symmetric positive definite matrix $\boldsymbol{Q}_b = \boldsymbol{Q}_b{}^T > \boldsymbol{0}$, there exists a symmetric positive definite matrix $\boldsymbol{P}_b = \boldsymbol{P}_b{}^T > \boldsymbol{0}$ that satisfies the Lyapunov equation,

$$\dot{\boldsymbol{P}}_b + \boldsymbol{A}_{ro}{}^T\boldsymbol{P}_b + \boldsymbol{P}_b\boldsymbol{A}_{ro} = -\boldsymbol{Q}_b. \tag{85}$$

Theorem 2. *Let the inequality (86) holds. Then, the equilibrium point of the dynamic system with uncertainties stated in (76) is asymptotically stable.*

$$\Upsilon < \frac{\lambda_{\min}(\boldsymbol{Q}_b)}{2\lambda_{\max}(P_b)}. \tag{86}$$

Consider $V(\boldsymbol{e}_n) = \boldsymbol{e}_n^T\boldsymbol{P}_b\boldsymbol{e}_n$ as a Lyapunov function candidate for a system (80). The derivative of the Lyapunov function can be written as,

$$\begin{aligned}\dot{V}(\boldsymbol{e}_n) &= -\boldsymbol{e}_n\boldsymbol{e}_n{}^T\boldsymbol{Q}_b + \boldsymbol{B}_{ro}^T c_e^T\boldsymbol{P}_b\boldsymbol{e}_n + \boldsymbol{e}_n^T\boldsymbol{P}_b\boldsymbol{B}_{ro}\boldsymbol{v}.\\ &\le -\lambda_{\min}(\boldsymbol{Q}_b)\ ||\boldsymbol{e}_n||^2 + 2\gamma\lambda_{\max}(\boldsymbol{P}_b)||\boldsymbol{e}_n||^2\\ &\le -(\lambda_{\min}(\boldsymbol{Q}_b) - 2\gamma\lambda_{\max}(\boldsymbol{P}_b))||\boldsymbol{e}_n||^2,\end{aligned} \tag{87}$$

which is negative if $\Upsilon < \frac{\lambda_{\min}(\boldsymbol{Q}_b)}{2\lambda_{\max}(P_b)}$. This proves the asymptotic stability of the system.

5.2. SMC

According to Slotine and Li [46], Zheng et al. [58], to solve the tracking control issue, the trajectory on the sliding surface is maintained as $s(t) = 0$ and the sliding surface vector is defined as,

$$\boldsymbol{\sigma}(\boldsymbol{e}_n) = \dot{\boldsymbol{e}}_{n1} + \boldsymbol{\Lambda}\boldsymbol{e}_{n1} = \boldsymbol{S}\ \boldsymbol{e}_n, \tag{88}$$

where $\boldsymbol{S} = \begin{bmatrix}\boldsymbol{\Lambda}\ \boldsymbol{I}\end{bmatrix}$. $\boldsymbol{\Lambda}$ is a diagonal matrix with positive scalars λ_i, $i = 1, 2, \cdots, 5$ and $\boldsymbol{I}$ is the identity matrix. Here, a virtual torque $\bar{\boldsymbol{\tau}}_R^\star = \bar{\boldsymbol{M}}_{ORR}^{*-1}\bar{\boldsymbol{\tau}}_R$ is assigned to decouple the multiple torque inputs. The rigid motion of SRFM defined in (52) can be written as,

$$\dot{\boldsymbol{e}}_{n2} = -\bar{\boldsymbol{M}}_{RR}^{-1*}\bar{\boldsymbol{C}}_{RR}^*\dot{\bar{\boldsymbol{p}}}_s - \ddot{\bar{\boldsymbol{p}}}_d + \bar{\boldsymbol{M}}_{RR}^{*-1}\boldsymbol{M}_{ORR}\bar{\boldsymbol{\tau}}_R^\star. \tag{89}$$

By using $\bar{\boldsymbol{M}}_{RR}^* = \bar{\boldsymbol{M}}_{ORR}^* + \Delta\bar{\boldsymbol{M}}_{RR}^*$, (89) can be written as,

$$\begin{aligned}\dot{\boldsymbol{e}}_{n2} &= -\bar{\boldsymbol{M}}_{RR}^{*-1}\bar{\boldsymbol{C}}_{RR}^*\dot{\bar{\boldsymbol{p}}}_s - \ddot{\bar{\boldsymbol{p}}}_d + \bar{\boldsymbol{M}}_{RR}^{*-1}\left(\bar{\boldsymbol{M}}_{RR}^* - \Delta\bar{\boldsymbol{M}}_{RR}^*\right)\bar{\boldsymbol{\tau}}_R^\star\\ &= \bar{\boldsymbol{f}}(\boldsymbol{e}_n, t) + \bar{\boldsymbol{\tau}}_R^\star + \bar{\boldsymbol{g}}(\boldsymbol{e}_n, t),\end{aligned} \tag{90}$$

where $\bar{\boldsymbol{f}}(\boldsymbol{e}_n, t) = -\bar{\boldsymbol{M}}_{RR}^{*-1}\bar{\boldsymbol{C}}_{RR}^*\dot{\bar{\boldsymbol{p}}}_s - \ddot{\bar{\boldsymbol{p}}}_d$ and $\bar{\boldsymbol{g}}(\boldsymbol{e}_n, t) = -\bar{\boldsymbol{M}}_{RR}^{*-1}\Delta\bar{\boldsymbol{M}}_{RR}^*\bar{\boldsymbol{\tau}}_R$.

Different positive scalars $\bar{\pi}, p_1, p_2, q_1, q_2, r_1, r_2$ are used to define system uncertainties for deriving the control law as follows:

$$\begin{aligned}&||\bar{\boldsymbol{M}}_{RR}^* - \bar{\boldsymbol{M}}_{ORR}^*|| = ||\Delta\bar{\boldsymbol{M}}_{RR}^*|| \le \bar{\pi}\,||\bar{\boldsymbol{M}}_{ORR}^*||,\\ &\quad||p_1||\bar{\boldsymbol{M}}_{ORR}^*|| \le ||\bar{\boldsymbol{M}}_{RR}^*|| \le p_2||\bar{\boldsymbol{M}}_{ORR}^*||,\\ &\quad q_1||\bar{\boldsymbol{C}}_{ORR}^*|| \le ||\bar{\boldsymbol{C}}_{RR}^*|| \le q_2||\bar{\boldsymbol{C}}_{ORR}^*||,\\ &\quad r_1||\bar{\boldsymbol{M}}_{ORR}^{*-1}|| \le ||\bar{\boldsymbol{M}}_{RR}^{*-1}|| \le r_2||\bar{\boldsymbol{M}}_{ORR}^{*-1}||.\end{aligned}$$

The difference between the actual values and their nominal values of $\bar{\boldsymbol{f}} - \hat{\boldsymbol{f}}$ and $\bar{\boldsymbol{g}} - \hat{\boldsymbol{g}}$ can be obtained as,

$$\begin{aligned}&||\bar{\boldsymbol{f}} - \hat{\boldsymbol{f}}|| \le (q_2r_2 + 1)||\bar{\boldsymbol{M}}_{ORR}^{*-1}||\ ||\bar{\boldsymbol{C}}_{ORR}^*||\ ||\boldsymbol{e}_{n2} + \dot{\boldsymbol{p}}_d|| = \boldsymbol{f}^\star,\\ &||\bar{\boldsymbol{g}} - \hat{\boldsymbol{g}}|| = ||\boldsymbol{g}|| \le q_2\bar{\pi}||\bar{\boldsymbol{M}}_{ORR}^{*-1}||\ ||\bar{\boldsymbol{M}}_{ORR}^*||\ ||\bar{\boldsymbol{M}}_{ORR}^{*-1}||\bar{\boldsymbol{\tau}}_{\text{Rmax}} = \boldsymbol{g}^\star,\end{aligned} \tag{91}$$

where $\bar{\boldsymbol{\tau}}_{\text{Rmax}}$ is the maximum of the absolute value of output torque. The virtual torque for rigid motion is computed as,

$$\bar{\tau}_{Ri}^\star = -\lambda_i e_{n2i} + \ddot{p}_{di} - \hat{f}_i - \hat{g}_i - \left(f_i^\star + g_i^\star + \alpha_i\right)\ \text{sat}(\sigma_i), \tag{92}$$

where α is a small positive scalar. From (92), the actual torque for rigid motion control can be derived as $\bar{\boldsymbol{\tau}}_R = \bar{\boldsymbol{M}}_{ORR}^*\bar{\boldsymbol{\tau}}_R^\star$. The detailed formulation of this control method and stability proof can be found in [44].

5.3. Linear quadratic regulator

As (58) is in a linear feedback form, LQR control law is developed to control the flexible motion. It can be seen from (17) and (42), $\tilde{\boldsymbol{K}}_{FF}$, $\bar{\boldsymbol{W}}_{FF}^*$, and $\bar{\boldsymbol{W}}_{FR}^*$ are non-singular matrices. Therefore, the pair ($\boldsymbol{A}_{FS}$, $\boldsymbol{B}_{FS}$) is completely controllable and stable. The main objective of the LQR scheme is to compute the optimal feedback gain by minimizing the cost function $\boldsymbol{J}_c$ given as,

$$\boldsymbol{J}_c = \frac{1}{2}\int_0^\infty \left(\boldsymbol{fs}^T\boldsymbol{Q}_{FS}\boldsymbol{fs} + \boldsymbol{\tau}_{FS}^T\boldsymbol{R}_{FS}\boldsymbol{\tau}_{FS}\right)dt_f, \tag{93}$$

where $\boldsymbol{Q}_{FS}$ and $\boldsymbol{R}_{FS}$ are the design parameters to penalize the state variables and the control signals, respectively. In the LQR method, $\boldsymbol{Q}_{FS}$ and $\boldsymbol{R}_{FS}$ are essential elements in deriving the control input. The optimal feedback gain $\boldsymbol{K}_{Fgain}$ is obtained by solving the following Algebraic Riccati Equation (ARE),

$$\boldsymbol{A}_{FS}^T\boldsymbol{P}_{FS} + \boldsymbol{P}_{FS}\boldsymbol{A}_{FS} - \boldsymbol{P}_{FS}\boldsymbol{B}_{FS}\boldsymbol{R}_{FS}^{-1}\boldsymbol{B}_{FS}^T\boldsymbol{P}_{FS} + \boldsymbol{Q}_{FS} = \boldsymbol{0}, \tag{94}$$

where $\boldsymbol{P}_{FS}$ is a positive definite matrix. The optimal feedback control law that minimizes the above cost function, given in (93), is computed as,

$$\boldsymbol{\tau}_{FS} = -\boldsymbol{K}_{Fgain}\boldsymbol{fs}, \tag{95}$$

where, $\boldsymbol{K}_{Fgain}$ is given by,

$$\boldsymbol{K}_{Fgain} = \boldsymbol{R}_{FS}^{-1}\boldsymbol{B}_{FS}^T\boldsymbol{P}_{FS}. \tag{96}$$

After deriving the control inputs $\bar{\boldsymbol{\tau}}_R$ for the rigid part and $\bar{\boldsymbol{\tau}}_{FS}$ for the flexible part, after the impact with an external object, the summation of these two control inputs are applied to the post-impact dynamic system to evaluate the performance of the system. This composite control guarantees the stability of closed-loop SRFM. The stability of the proposed composite controllers, NMPC-LQR and SMC-LQR will minimize the tracking error of the system.

6. Simulation

The highly nonlinear, coupled dynamics and system uncertainties of SRFM in space environment make their control design difficult. Therefore, to make control design simpler as previously explained, a planar two-link flexible space manipulator mounted on a spacecraft base as shown in Fig. 1 as in [26] is used in this study. The effectiveness of the proposed control algorithms to stabilize

Table 1
Parameters of a spacecraft with flexible manipulator.

Parameter	Symbol	Value	Unit
Spacecraft mass	m_b	10	kg
Mass of link 1	m_{L1}	2	kg
Mass of link 2	m_{L2}	2	kg
Mass of hub	m_h	1	kg
Mass of payload	m_p	0.1	kg
Length between o_1 and o_2	o_1o_2	0.5	m
Length of link 1	L_1	2	m
Length of link 2	L_2	2	m
Inertia of spacecraft base	I_b	10	kg.m^2
Inertia of hub	I_h	1	kg.m^2
Inertia of payload	I_p	0.1	kg.m^2
Rigidity for first link	EI_1	50	Nm^2
Rigidity for second link	EI_2	50	Nm^2

Table 2
Initial condition of the system.

Parameter	Symbol	Value	Unit
Position of spacecraft-base	$[\boldsymbol{x}_b, \boldsymbol{y}_b]^T$	$[0.2, -0.2]^T$	m
Attitude angle of spacecraft	$\boldsymbol{\theta}_0$	10	$^\circ$
Position of end-effector	$[\boldsymbol{x}_{ep}, \boldsymbol{y}_{ep}]^T$	$[4.3941, 1.1914]^T$	m
Linear velocity of SRFM	$\boldsymbol{v}$	$\mathbf{0}$	m/s
Angular velocity of SRFM	$\boldsymbol{\omega}$	$\mathbf{0}$	$^\circ/s$

the post-impact stage of the system is demonstrated via numerical simulations. The desired trajectory of the SRFM is described by using a fifth-degree polynomial because, according to Khalil and Dombre [27], it guarantees the continuity of velocity and acceleration. The mass of the external object $m_o = 2.5\ kg$ is chosen. The initial linear velocity and angular velocity of the object are taken as $[-0.4; 0.4]\ m/s$ and $0.2\ rad/s$, respectively. It is assumed the external object impacts the space robot system at $5s$ of simulation time for $0.3s$ and all states are in desired values before the impact. This assumption is reasonable in practice when a space robot impacts with another spacecraft and space robot in the space environment. The specific parameters of the system and the initial conditions used in the simulation are shown in Tables 1 and 2, respectively.

6.1. Simulation results using NMPC-LQR and SMC-LQR

This section shows simulation results of SRFM using NMPC-LQR and compared to SMC-LQR, in the absence of uncertainties. The composite controller SMC-LQR was proposed in [26] to control the post-impact motion of the SRFM. However, the magnitude of the flexible displacement for both links using SMC-LQR is more than $3mm$. In addition, the orientation tracking error of the spacecraft is of the order of 10^{-4} radian. This error might cause a problem while performing some special tasks in the space environment that require higher accuracy such as fuelling, painting etc. In [25], it was seen that the NMPC method provides higher accuracy for rigid motion response of the system compared to the SMC method. Hence, the performance of the SRFM for both rigid and flexible motion using the proposed composite controller NMPC-LQR is compared with the SMC-LQR given in [26]. The control parameters used for the simulation are given in Table 3. They are chosen by trial and error method until the system responds with better performance by minimizing the error.

The trajectory tracked by the end-effector of the SRFM using the proposed composite controllers, NMPC-LQR and SMC-LQR is compared with the desired trajectory and is shown in Fig. 2, which shows that both the proposed controllers effectively track the desired end-effector trajectory. Although both controllers successfully track the desired trajectory, the performance tracking errors of SRFM are also examined. The position tracking and attitude

Table 3
Control parameters used in simulation for NMPC-LQR and SMC-LQR.

Controller	Description	Value
NMPC-LQR	State weight matrix ($\boldsymbol{Q}_p$)	$10^5\boldsymbol{I}_{(5\times5)}$
	Control weight matrix ($\boldsymbol{R}_p$)	$10^{-7}\boldsymbol{I}_{(5\times5)}$
	Time increment (T_s)	$0.01\ s$
	State weight matrix ($\boldsymbol{Q}$)	$100\begin{bmatrix} 100*\boldsymbol{I}_{4\times4} & \mathbf{0}_{4\times4} \\ \mathbf{0}_{4\times4} & \boldsymbol{I}_{4\times4} \end{bmatrix}$
	Control weight matrix ($\boldsymbol{R}$)	$0.1\begin{bmatrix} \boldsymbol{I}_{3\times3} & \mathbf{0}_{3\times2} \\ \mathbf{0}_{2\times3} & 10*\boldsymbol{I}_{2\times2} \end{bmatrix}$
SMC-LQR	Positive scalar (α_i)	0.001
	Sliding manifold parameter (Λ_i)	1
	Positive scalars ($\tilde{\pi}$)	0.3
	Positive scalars ($\tilde{p}_1 = \tilde{q}_1 = \tilde{r}_1$)	0.2
	Positive scalars ($\tilde{p}_2 = \tilde{q}_2 = \tilde{r}_2$)	1.8
	Boundary layer thickness (ε_i)	0.24
	State weight matrix ($\boldsymbol{Q}$)	$100\begin{bmatrix} 100*\boldsymbol{I}_{4\times4} & \mathbf{0}_{4\times4} \\ \mathbf{0}_{4\times4} & \boldsymbol{I}_{4\times4} \end{bmatrix}$
	Control weight matrix ($\boldsymbol{R}$)	$0.1\begin{bmatrix} \boldsymbol{I}_{3\times3} & \mathbf{0}_{3\times2} \\ \mathbf{0}_{2\times3} & 10*\boldsymbol{I}_{2\times2} \end{bmatrix}$

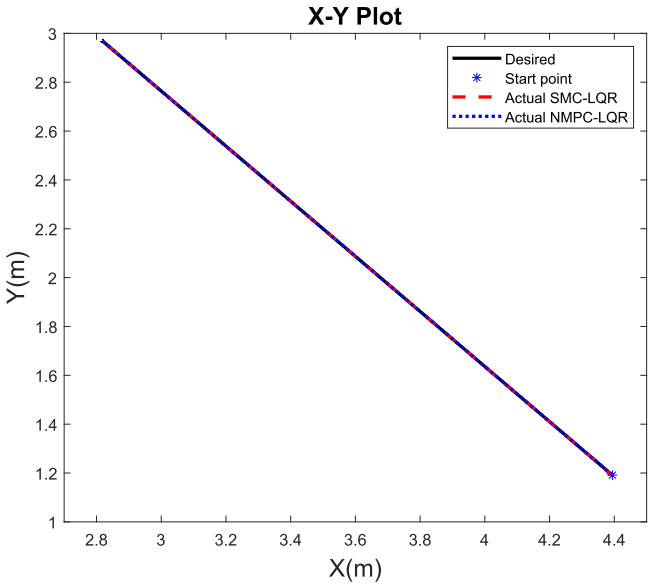

Fig. 2. XY plot for an end-effector: both the proposed controllers effectively track the desired end-effector trajectory.

tracking errors of the spacecraft base using composite controllers namely NMPC-LQR and SMC-LQR are shown in Fig. 3. It can be noticed that, at the time of impact the magnitude of error increases considerably. Even though the system is disturbed by the impact of the external object, both the proposed controllers NMPC-LQR and SMC-LQR track the desired position of the spacecraft successfully with an accuracy of the order of $10^{-6}m$ and $10^{-3}m$, respectively. Similarly, the magnitude of attitude tracking error for NMPC-LQR is of the order of 10^{-4} *degrees* and 0.02 *degrees* for SMC-LQR. From these simulation results, it is clear that the composite controller NMPC-LQR has higher accuracy for trajectory tracking of the spacecraft base than SMC-LQR. However, the magnitude of error of both proposed controllers is within acceptable limits to collect solar energy and communication of the ground system by the spacecraft base as the magnitude of attitude tracking only deviates by a small value.

Fig. 4a presents the position tracking error of the end-effector for x and y positions. Due to the impact, the magnitude of y increases remarkably. It can be seen that the magnitude of error for both the x and y positions is small for both controllers. They are of the order of $10^{-5}\ m$ and $10^{-3}\ m$, which are acceptable performance for most space robot tasks. The flexible displacement of

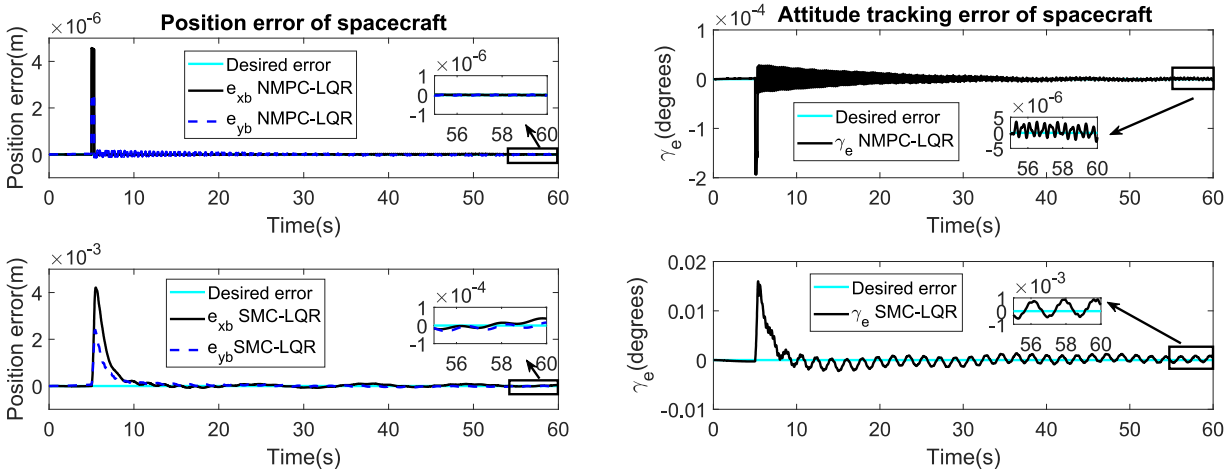

(a) Position tracking error (b) Attitude tracking error

Fig. 3. Trajectory tracking error of spacecraft after the impact. Figure 3(a) illustrates tracking error of the spacecraft in x and y position using NMPC-LQR and SMC-LQR, respectively. Figure 3(b) represents tracking error of the spacecraft in attitude using NMPC-LQR and SMC-LQR, respectively. NMPC-LQR has less tracking errors compared to SMC-LQR.

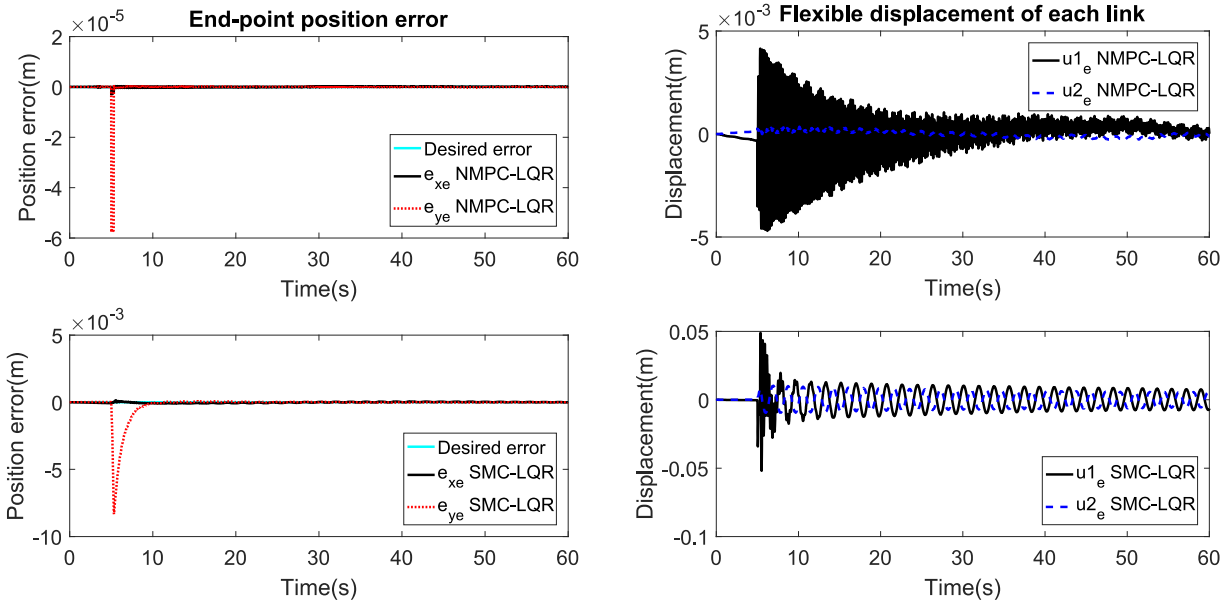

(a) End-point position tracking error (b) Flexible deflection of each link

Fig. 4. End-point position tracking error and flexible deflection after the impact. Figure 4(a) shows tracking error of the end-effector in x and y positions using NMPC-LQR and SMC-LQR, respectively. Figure 4(b) illustrates the flexible displacement of link 1 and link 2 using NMPC-LQR and SMC-LQR, respectively. The magnitude of tracking error responses using NMPC-LQR is less than SMC-LQR.

link 1 and link 2 is depicted in Fig. 4b. It can be noted that the magnitude of flexible displacement by using composite controller NMPC-LQR is smaller than that of SMC-LQR. The flexible displacement of the first link is higher than that of the second link for both composite controllers as the impact force is applied at the end-effector. The magnitude of flexible displacements using NMPC-LQR decreases slowly throughout the simulation, being approximately $1mm$ and $0.5mm$ for link 1 and link 2, respectively. As we know, it is normal to have vibration of small magnitude of the flexible structure even though control input is applied in the system. Here, these flexible displacements are minimal and do not affect most space robot missions such as fueling, painting, assembling structures, collecting samples for examination. On the other hand, using SMC-LQR, the magnitude of flexible displacements remains almost the same throughout the simulation time, being about $5mm$ and $3mm$ for link 1 and link 2, respectively. These magnitudes of flexible displacement is small enough to carry out some of the special tasks in a space robot mission such as removal of space debris, collection of disabled satellites, inspection of space structures, exploration of space environment etc. which does not require higher accuracy. However, for higher accuracy missions, NMPC-LQR can be used as it provides the vibration of less than $1mm$.

Structural damping was neglected in the simulations in order to avoid complexity in deriving the dynamic equations and design-

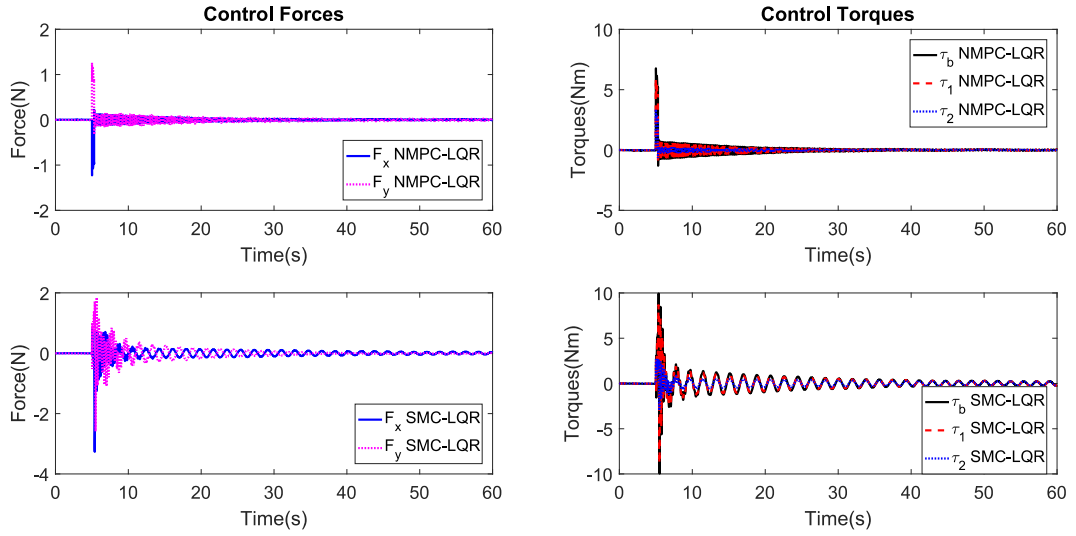

(a) Control forces (b) Control torques

Fig. 5. Control inputs after the impact. Figure 5(a) depicts control forces applied to the system using NMPC-LQR and SMC-LQR, respectively. Figure 5(b) reveals control torques applied to the system using NMPC-LQR and SMC-LQR, respectively. SMC-LQR requires higher magnitude of control inputs compared to NMPC-LQR.

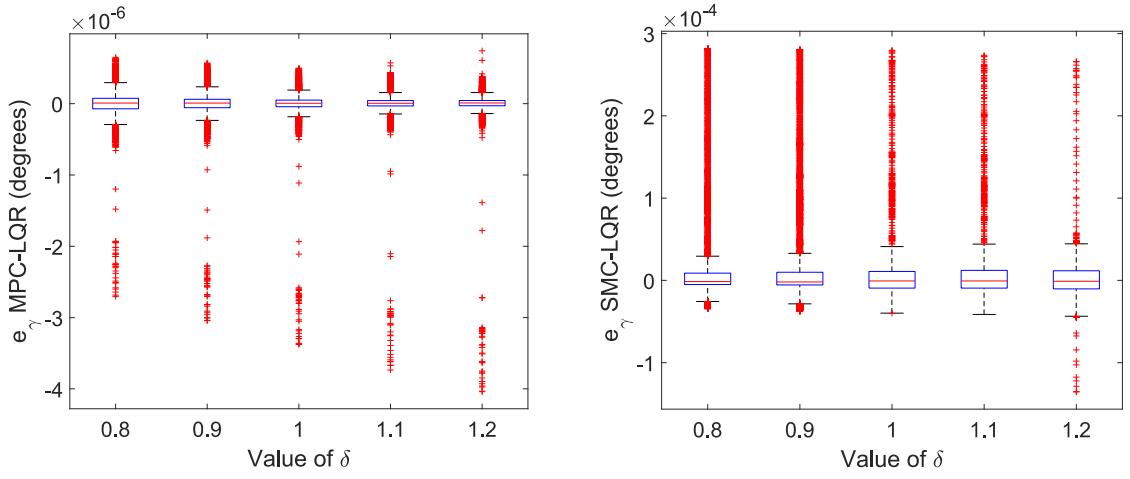

(a) Attitude error using MPC-LQR (b) Attitude error using SMC-LQR

Fig. 6. Attitude error with system uncertainty. Figure 6(a) depicts boxplot of attitude error of spacecraft base using NMPC-LQR. Figure 6(b) illustrates boxplot of attitude error of spacecraft base using SMC-LQR. NMPC-LQR provides less magnitude of errors compared to SMC-LQR.

ing effective control law hence, the flexible displacements oscillate throughout the entire simulation. As flexible links are not the same as rigid links, it is normal to get small oscillations. The simulation results show the oscillations are of small magnitude and they are acceptable to perform many space robot applications such as explorations, transporting objects from one position to another.

The control inputs applied to the system are shown in Fig. 5. Here again, due to impact, the magnitude of the control inputs increases significantly at the time of impact, then settles down slowly. The magnitude of applied control inputs to the system is in the practical range as described in [45,51]. To compare the performance of the system, the magnitude of the control inputs were kept in a similar range for both controllers. However, the magnitude of the control inputs for SMC-LQR is slightly greater than that of NMPC-LQR. From simulation results, we notice that the composite controller NMPC-LQR provides better performance with higher accuracy compared to SMC-LQR even though similar magnitude of control inputs are applied to the system.

6.2. Simulation results using NMPC-LQR and SMC-LQR in the presence of uncertainty

To investigate the robustness of the controllers, simulations were also carried out in the presence of uncertainties. For this, the coefficient δ is used to define the uncertainties on mass and inertia of the SRFM:

$$m_s = \delta m_s, I_s = \delta I_s, \tag{97}$$

where m_s, I_s are the actual values of mass and moment of inertia of the SRFM, respectively. In this study, the uncertainty of an external object is not included in the control design as the moment of inertia of the external object cannot be determined. The offset

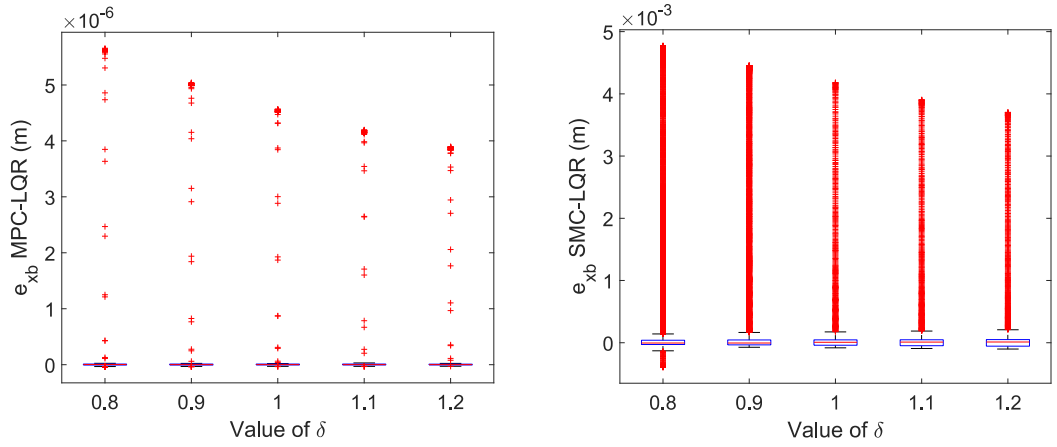

(a) x-position error using MPC-LQR (b) x-position error using SMC-LQR

Fig. 7. x-position tracking error with system uncertainty. Figure 7(a) represents boxplot of x-position tracking error of spacecraft base using NMPC-LQR. Figure 7(b) shows boxplot of x-position tracking error of spacecraft base using SMC-LQR. The errors using SMC-LQR are higher that that of NMPC-LQR.

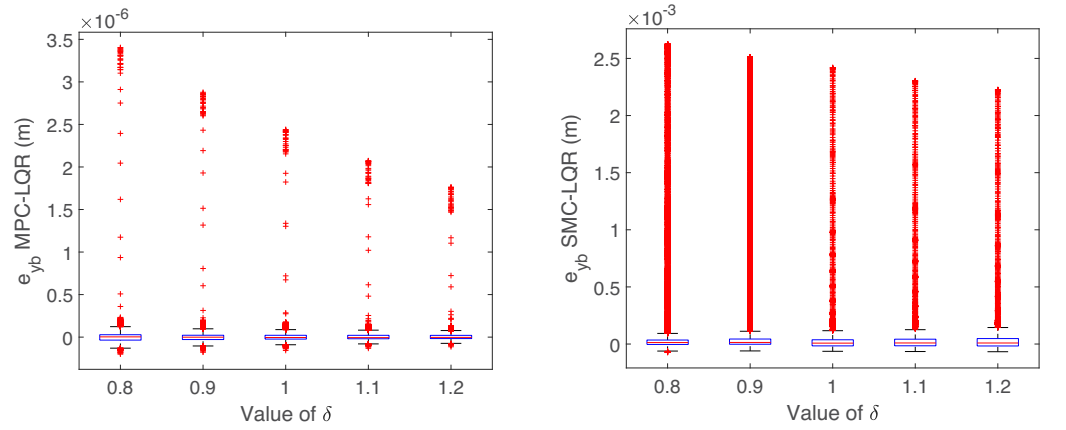

(a) y-position error using MPC-LQR (b) y-position error using SMC-LQR

Fig. 8. y-position tracking error with system uncertainty. Figure 8(a) depicts boxplot of y-position tracking error of spacecraft base using NMPC-LQR. Figure 8(b) represents boxplot of y-position tracking error of spacecraft base using SMC-LQR. SMC-LQR provides higher magnitude of errors compared to NMPC-LQR.

values of δ are set within the range $\delta \in [-0.2, 0.2]$ for each simulation.

To show a better comparison of the two controllers on the SRFM in the presence of uncertainty, the simulation results are illustrated via a boxplot, which gives minimum, first quartile, median, third quartile, maximum and outlier. In the boxplot, the horizontal red lines inside the box indicate the median of the data and the red points represent the outlier. A red line closer to zero means a better result. The upper and lower blue lines are first and third quartile, respectively.

Fig. 6 indicates the boxplot of the attitude tracking error of the spacecraft base in the presence of uncertainty under both NMPC-LQR and SMC-LQR methods. As shown in the figure, the median error of NMPC-LQR is of the order of 1×10^2 magnitude smaller than that obtained with the SMC-LQR method. In the same way, the boxplots of x-position and y-position tracking error of spacecraft base using NMPC-LQR and SMC-LQR are presented in Figs. 7 and 8, respectively. Here, again the median error of NMPC-LQR is small compared to SMC-LQR in both x and y positions of the spacecraft base. With increasing value of δ, the error decreases whether using NMPC-LQR or SMC-LQR.

Likewise, as shown in Figs. 9 and 10, the boxplot of the position tracking errors of the end-effector for NMPC-LQR is 1×10^2 magnitude less compared to the SMC-LQR method. The boxplots of flexible displacement of link 1 and link 2 are given in Figs. 11 and 12, respectively using NMPC-LQR and SMC-LQR in the presence of uncertainty. The median error for link 2 using NMPC-LQR is 1×10^2 magnitude less than SMC-LQR method. However, the median error for link 1 using SMC-LQR is 0.016 magnitude more than that of NMPC-LQR. From this simulation results, it can be said that NMPC-LQR has better performance compared to SMC-LQR whether uncertainties are included or not in the system. The position and orientation tracking error of spacecraft base and position tracking error of end-effector are always less using NMPC-LQR than SMC-LQR.

Overall, the simulation results show that the uncertainty of mass and inertia on SRFM has little effect on the performance of either composite controllers NMPC-LQR or SMC-LQR. The magnitude of the error is in the same range using NMPC-LQR controller whether uncertainties are included or not in the system. Similarly, SMC-LQR also provides the same magnitude of error whether uncertainties are included or not in the system. Therefore, it can be

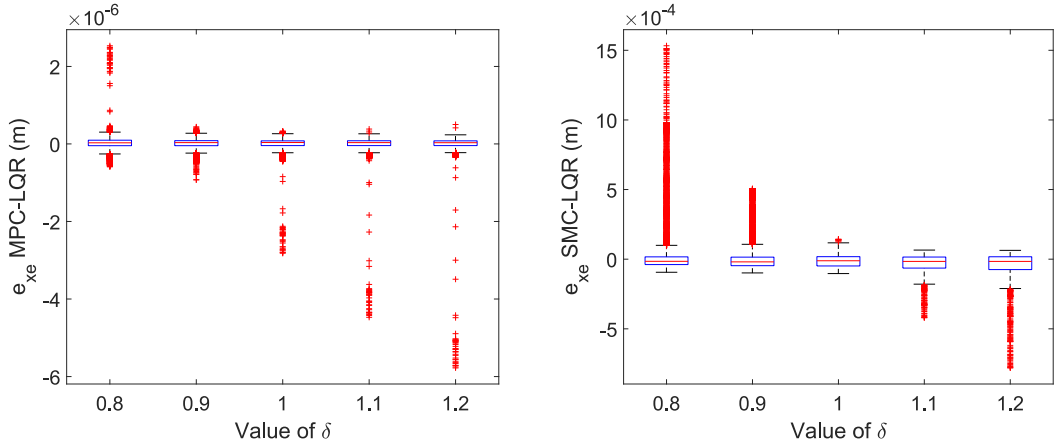

(a) Endpoint x-position error using MPC-LQR (b) Endpoint x-position error using SMC-LQR

Fig. 9. Endpoint x-position tracking error with system uncertainty. Figure 9(a) shows boxplot of x-position tracking error for endpoint position using NMPC-LQR. Figure 9(b) illustrates boxplot of x-position tracking error for endpoint position using SMC-LQR. NMPC-LQR provides higher accuracy compared to SMC-LQR.

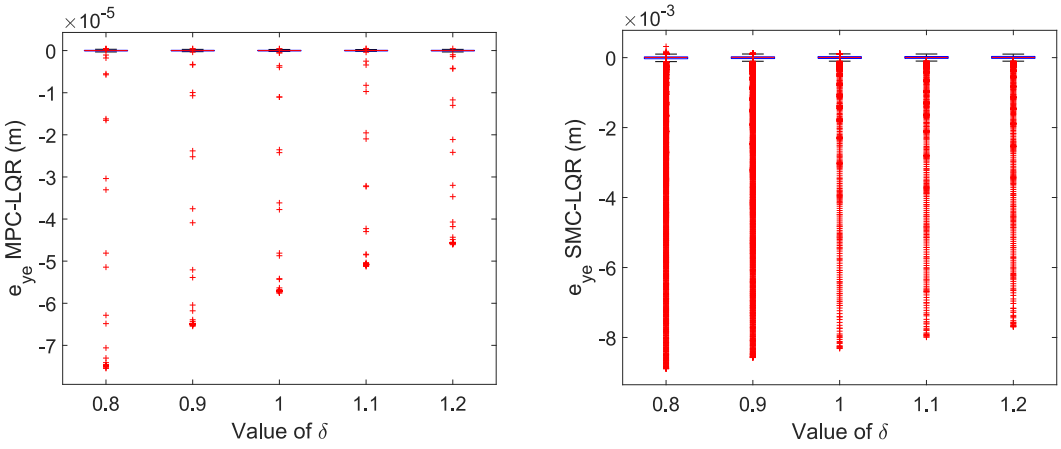

(a) Endpoint y-position error using MPC-LQR (b) Endpoint y-position error using SMC-LQR

Fig. 10. Endpoint y-position tracking error with system uncertainty. Figure 10(a) reveals boxplot of endpoint y-position tracking error using NMPC-LQR. Figure 10(b) depicts boxplot of endpoint y-position tracking error using SMC-LQR. NMPC-LQR has less error compared to SMC-LQR.

said that both controllers perform well in the presence of the parameter uncertainty considered in this study. However, the proposed controller NMPC-LQR has less tracking error meaning it has superior performance compared to SMC-LQR both in the presence and absence of uncertainties in the system. Based on the simulation results, it can be concluded that NMPC-LQR may be preferable for high accuracy tracking missions such as fuelling, painting etc. in space environment. This comparative study provides better knowledge on the use of control techniques for various space robots tasks.

7. Conclusion

In this paper, we explored post-impact motion control of a spacecraft with a two-link flexible manipulator. The key improvement in this model is that both links are flexible. The highly nonlinear dynamics of the system were segregated into rigid and flexible subsystem to make it simpler to design the control algorithm. Then, a composite controller NMPC-LQR was derived to control the unstable motion of the space robot system with flexible manipulator and the performance of the system was compared with the SMC-LQR control method. Through simulation it can be seen that both controllers effectively control the post-impact dynamics of a spacecraft even though it was disturbed by the motion of the robot manipulator. In addition, the robot manipulator successfully tracks the desired trajectory regardless of the external impact on the system. Moreover, it can be noticed that the performance of the system using NMPC-LQR is more accurate compared to that of SMC-LQR although a similar magnitude of control inputs were applied to the system in each case. This comparative study provides a better understanding of the selection of control law according to requirements such as higher accuracy. The robustness of both controllers was then evaluated by including uncertainties into the system. The results show that both the two controllers perform effectively with the provided uncertainties. However, NMPC-LQR provides excellent performance when compared to SMC-LQR both in the presence and absence of uncertainties.

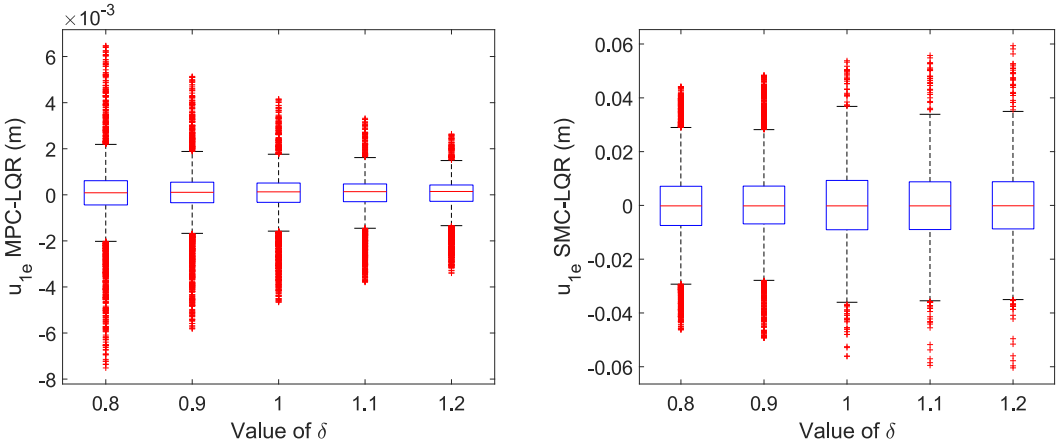

(a) Flexible displacement of link 1 using MPC-LQR (b) Flexible displacement of link 1 using SMC-LQR

Fig. 11. Flexible displacement of link 1 with system uncertainty. Figure 11(a) depicts boxplot of flexible displacement of link 1 using NMPC-LQR. Figure 11(b) illustrates boxplot of flexible displacement of link 1 using SMC-LQR. The errors using SMC-LQR are higher than NMPC-LQR.

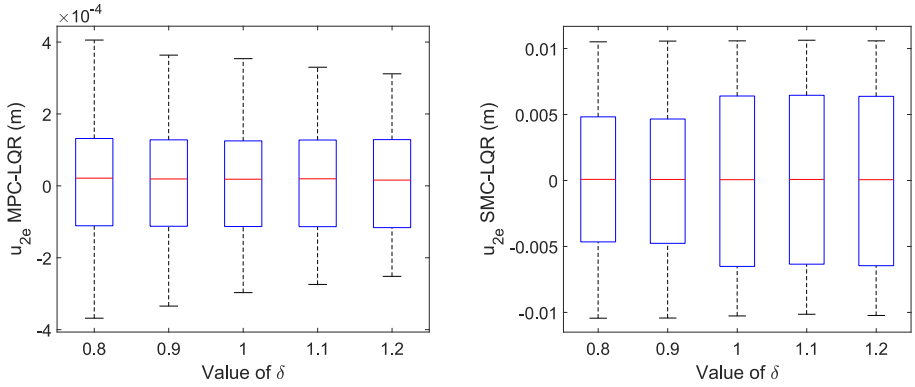

(a) Flexible displacement of link 2 using MPC-LQR (b) Flexible displacement of link 2 using SMC-LQR

Fig. 12. Flexible displacement of link 2 with system uncertainty. Figure 12(a) shows boxplot of flexible displacement of link 2 using NMPC-LQR. Figure 12(b) represents boxplot of flexible displacement of link 2 using SMC-LQR. NMPC-LQR provides better performance compared to SMC-LQR.

For future work, the performance of the proposed composite controller can be compared with other adaptive controllers and different variants of SMC. Moreover, to study the full performance of the SRFM, this research needs to be extended by considering 6DoF motion in the space environment and the robustness of the proposed controller investigated.

As we know, the space robot system might be impacted by external objects which damage the system if the impact forces are high. There is limited research on force control of the space robot system with a flexible manipulator. In this study, only motion control of the SRFM was considered. Therefore, force control could be considered for a space robot with the flexible manipulator, in future research.

Declaration of Competing Interest

The authors declare that they have no known competing financial interests or personal relationships that could have appeared to influence the work reported in this paper.

References

[1] K. Bdirina, R. Hajer, M. Boucherit, D. Djoudi, D. Rabehi, One step ahead nonlinear predictive control of two links robot manipulators, in: International Symposium on Power Electronics, Electrical Drives, Automation and Motion (SPEEDAM), 2012, pp. 1219–1223.

[2] G. Chen, D. Liu, Y. Wang, Q. Jia, X. Liu, Contact force minimization for space flexible manipulators based on effective mass, J. Guid. Control Dyn. 42 (8) (2019) 1870–1877.

[3] Y. Chen, L. Meirovitch, Control of a flexible space robot executing a docking maneuver, J. Dyn. Syst. Meas. Control 18 (4) (1995) 756–766, doi:10.2514/3.21457.

[4] M. Chien, A. Huang, Adaptive control for flexible-joint electrically driven robot with time-varying uncertainties, IEEE Trans. Ind. Electron. 54 (2) (2007) 1032–1038, doi:10.1109/TIE.2007.893054.

[5] F. Curti, M. Romano, R. Bevilacqua, Lyapunov-based thrusters' selection for spacecraft control: analysis and experimentation, J. Guid. Control Dyn. 33 (4) (2010) 1143–1160, doi:10.2514/1.47296.

[6] D. Dimitrov, K. Yoshida, Momentum distribution in a space manipulator for facilitating the post-impact control, in: 2004 IEEE/RSJ International Conference on Intelligent Robots and Systems (IROS) (IEEE Cat. No. 04CH37566), vol. 4, 2004, pp. 3345–3350, doi:10.1109/IROS.2004.1389933.

[7] Q. Dong, L. Chen, Impact dynamics analysis of free-floating space manipulator capturing satellite on orbit and robust adaptive compound control algorithm design for suppressing motion, Appl. Math. Mech. 35 (2010) (2014) 413–422, doi:10.1007/s10483-014-1801-7.

[8] S. Dubowsky, E. Papadopoulos, The kinematics, dynamics, and control of free-flying and free-floating space robotic systems, IEEE Trans. Rob. Autom. 9 (5) (1993) 531–543.

[9] S.K. Dwivedy, P. Eberhard, Dynamic analysis of flexible manipulators, a literature review, Mech. Mach. Theory 41 (7) (2006) 749–777.

[10] T. Fan, Intelligent model predictive control of flexible link robotic manipulators, University of British Columbia, 2007 Ph.D. thesis.

[11] T. Fan, C.W.D. Silva, Intelligent model predictive control of a flexible-link robotic manipulator, in: ASME 2005 International Mechanical Engineering Congress and Exposition, 2005, pp. 1019–1025.

[12] T. Fan, C.W.D. Silva, Dynamic modelling and model predictive control of flexible-link manipulators, Int. J. Rob. Autom. 23 (4) (2008), doi:10.2316/Journal.206.2008.4.206-3149.

[13] R. Findeisen, L. Imsland, F. Allgo, B.A. Foss, State and output feedback nonlinear model predictive control: an overview, Eur. J. Control (2003) 190–206.

[14] A. Flores-Abad, O. Ma, K. Pham, S. Ulrich, A review of space robotics technologies for on-orbit servicing, Prog. Aerosp. Sci. 68 (2014) 1–26, doi:10.1016/j.paerosci.2014.03.002.

[15] A.M. Giordano, C. Ott, A. Albu-Schäffer, Coordinated control of spacecraft's attitude and end-effector for space robots, IEEE Rob. Autom. Lett. 4 (2) (2019) 2108–2115.

[16] R. Hedjar, P. Boucher, Nonlinear receding-horizon control of rigid link robot manipulators, Int. J. Adv. Rob. Syst. 2 (1) (2005) 015–024, doi:10.5772/5806.

[17] T. Henmi, M. Deng, A. Inoue, Adaptive control of a two-link planar manipulator using nonlinear model predictive control, in: 2010 IEEE International Conference on Mechatronics and Automation (ICMA), 2010, pp. 1868–1873.

[18] T. Henmi, T. Ohta, M. Deng, A. Inoue, Tracking control of the two-link manipulator using nonlinear model predictive control, in: ICNSC'09: International Conference on Networking, Sensing and Control, 2009, pp. 761–766.

[19] K.S. Holkar, L.M. Waghmare, An overview of model predictive control, Int. J. Control Autom. 3 (4) (2010) 47–63.

[20] J. Hu, B. Ding, One-step ahead robust MPC for LPV model with bounded disturbance, Eur. J. Control 52 (2020) 59–66.

[21] P. Huang, D. Wang, F. Zhang, Z. Meng, Z. Liu, Postcapture robust nonlinear control for tethered space robot with constraints on actuator and velocity of space tether, Int. J. Robust Nonlinear Control 27 (16) (2017) 2824–2841, doi:10.1002/rnc.3712.

[22] P. Huang, Y. Xu, B. Liang, Contact and impact dynamics of space manipulator and free-flying target, in: 2005 IEEE/RSJ International Conference on Intelligent Robots and Systems, IROS, 2005, pp. 1935–1940, doi:10.1109/IROS.2005.1545260.

[23] Z. Jing, Q. Xu, J. Huang, A review on kinematic analysis and dynamic stable control of space flexible manipulators, Aerosp. Syst. 2 (1) (2019) 1–14.

[24] Y. Kawai, T. Endo, F. Matsuno, Cooperative control of large flexible space structure by two planar robots, IET Control Theory Appl. 15 (5) (2021) 771–783.

[25] S. Kayastha, L. Shi, J. Katupitiya, G. Pearce, Nonlinear model predictive control of a planar three-link space manipulator, in: Control Conference (ASCC), 2017 11th Asian, 2017, pp. 635–640, doi:10.1109/ASCC.2017.8287244.

[26] S. Kayastha, L. Shi, J. Katupitiya, G. Pearce, Post-impact motion control of a space robot with flexible manipulator, in: 2018 15th International Conference on Control, Automation, Robotics and Vision (ICARCV), 2018, pp. 710–715.

[27] W. Khalil, E. Dombre, Modeling Identification and Control of Robots, CRC Press, 2002.

[28] J.A. Lawrence, M.R. Stephen, Adaptive control of a flexible-link robotic manipulator with unknown payload dynamics, in: 1993 American Control Conference, 1993, pp. 2088–2092, doi:10.23919/ACC.1993.4793249.

[29] X. Li, L. Wu, Impact motion control of a flexible dual-arm space robot for capturing a spinning object, Int. J. Adv. Rob. Syst. 16 (3) (2019).

[30] S. Liu, L. Wu, Z. Lu, Impact dynamics and control of a flexible dual-arm space robot capturing an object, Appl. Math. Compuat. 185 (2007) 1149–1159, doi:10.1016/j.amc.2006.07.035.

[31] K. Lochan, B.K. Roy, B. Subudhi, A review on two-link flexible manipulators, Annu. Rev. Control 42 (2016) 346–367.

[32] P. Lu, Approximate nonlinear receding-horizon control laws in closed form, Int. J. Control 71 (1) (1998) 19–34.

[33] G. Ma, Z. Jiang, H. Li, J. Gao, Z. Yu, X. Chen, Y. Liu, Q. Huang, Hand-eye servo and impedance control for manipulator arm to capture target satellite safely, Robotica 33 (4) (2015) 848–864, doi:10.1017/S0263574714000587.

[34] R. Masoudi, M. Mahzoon, Maneuvering and vibrations control of a free-floating space robot with flexible arms, J. Dyn. Syst. Meas. Control 133 (5) (2011) 051001.

[35] L. Meirovitch, Y. Chen, Trajectory and control optimization for flexible space robots, J. Guid. Control Dyn. 18 (3) (1995) 493–502, doi:10.2514/3.21414.

[36] L. Meirovitch, S. Lim, Maneuvering and control of flexible space robots, J. Guid. Control Dyn. 17 (3) (1994) 520–528.

[37] D. Meng, Y. She, W. Xu, W. Lu, B. Liang, Dynamic modeling and vibration characteristics analysis of flexible-link and flexible-joint space manipulator, Multibody Syst. Dyn. 43 (4) (2018) 321–347.

[38] D.N. Nenchev, K. Yoshida, Impact analysis and post-impact motion control issues of a free-floating space robot subject to a force impulse, IEEE Trans. Rob. Autom. 15 (3) (1999) 548–557.

[39] E. Papadopoulos, F. Aghili, O. Ma, R. Lampariello, Robotic manipulation and capture in space: a survey, Front. Rob. AI 8 (2021) 228, doi:10.3389/frobt.2021.686723.

[40] P. Poignet, M. Gautier, Nonlinear model predictive control of a robot manipulator, in: 6th International Workshop on Advanced Motion Control. Proceedings, 2000, pp. 401–406.

[41] D. Raina, S. Gora, D. Maheshwari, S.V. Shah, Impact modeling and reactionless control for post-capturing and maneuvering of orbiting objects using a multi-arm space robot, Acta Astronaut. 182 (2021) 21–36, doi:10.1016/j.actaastro.2021.01.034.

[42] T. Rybus, K. Seweryn, J.Z. Sasiadek, Control system for free-floating space manipulator based on nonlinear model predictive control (NMPC), J. Intell. Rob. Syst. 85 (3) (2017) 491–509, doi:10.1007/s10846-016-0396-2.

[43] K. Senda, Y. Murotsu, Methodology for control of a space robot with flexible links, IEE Proc.-Control Theory Appl. 147 (6) (2000) 562–568.

[44] L. Shi, J. Katupitiya, N. Kinkaid, A robust attitude controller for a spacecraft equipped with a robotic manipulator, in: Proceedings of the American Control Conference 2016, 2016, pp. 4966–4971, doi:10.1109/ACC.2016.7526140.

[45] L. Shi, S. Kayastha, J. Katupitiya, Robust coordinated control of a dual-arm space robot, Acta Astronaut. 138 (2017) 475–489, doi:10.1016/j.actaastro.2017.06.009.

[46] J.J.E. Slotine, W. Li, Applied Nonlinear Control, Prentice Hall, 1991. first ed.

[47] D. Stansbery, J. Cloutier, Position and attitude control of a spacecraft using the state-dependent Riccati equation technique, in: Proceedings of the 2000 American Control Conference. ACC (IEEE Cat. No.00CH36334), vol. 3, 2000, pp. 1867–1871, doi:10.1109/ACC.2000.879525.

[48] H.A. Talebi, R.V. Patel, K. Khorasani, Control of Flexible-Link Manipulators using Neural Networks, Vol. 261, Springer Science & Business Media, 2001.

[49] R.J. Theodore, A. Ghosal, Comparison of the assumed modes and finite element models for flexible multilink manipulators, Int. J. Rob. Res. 14 (2) (1995) 91–111.

[50] A. Waqar, M. Adeel, A. Khurram, J. Usman, A.A. Soltan, I. Jamshed, Nonlinear control of a flexible joint robotic manipulator with experimental validation, Strojniški Vestnik-J. Mech. Eng. 64 (2018) 47–55.

[51] X. Yang, S.S. Ge, W. He, Dynamic modelling and adaptive robust tracking control of a space robot with two-link flexible manipulators under unknown disturbances, Int. J. Control 91 (4) (2017) 969–988, doi:10.1080/00207179.2017.1300837.

[52] X. Yang, S.S. Ge, J. Liu, Dynamics and noncollocated model-free position control for a space robot with multi-link flexible manipulators, Asian J. Control 21 (2) (2019) 714–724.

[53] K. Yoshida, Space robot dynamics and control: a historical perspective, J. Rob. Mechatron. 12 (4) (2000) 402–410.

[54] X.Y. Yu, Augmented robust control of a free-floating flexible space robot, proceedings of the institution of mechanical engineers, J. Aerosp. Eng. Part G 229 (5) (2015) 947–957.

[55] X.Y. Yu, L. Chen, Modeling and observer-based augmented adaptive control of flexible-joint free-floating space manipulators, Acta Astronaut. 108 (2015a) 146–155, doi:10.1016/j.actaastro.2014.12.002.

[56] X.Y. Yu, L. Chen, Singular perturbation augmented robust control and vibration suppression of free-floating flexible space manipulators, in: Proceedings of the 14th IFToMM World Congress, 2015b, pp. 211–216.

[57] Z. Zhang, W.Q. Wang, S. Siddiqui, Predictive function control of a two-link robot manipulator, in: Mechatronics and Automation, 2005 IEEE International Conference, vol. 4, 2005, pp. 2004–2009.

[58] K. Zheng, Y. Hu, B. Wu, Intelligent fuzzy sliding mode control for complex robot system with disturbances, Eur. J. Control 51 (2020) 95–109.